Department of Physics and Astronomy
Heidelberg University

Bachelor Thesis in Physics
submitted by

Jonathan Notter

born in Tübingen (Germany)

2024

Design and implementation of a superconducting tuning coil for the Penning-trap experiment ELCOTRAP

This Bachelor Thesis has been carried out by Jonathan Notter at the
Max-Planck-Institut für Kernphysik in Heidelberg
under the supervision of
Prof. Dr. Klaus Blaum and Jost Herkenhoff

Abstract

The increasing precision of Penning-trap experiments requires the development of novel cooling techniques to cool particles down to their motional ground state. One promising approach for ions that cannot be laser cooled is sympathetic cooling using a self-cooled electron cloud. This approach is currently under investigation in the ELCOTRAP experiment at the *Max Planck Institute for Nuclear Physics* (MPIK).

In this work, a superconducting B_0-tuning coil for ELCOTRAP is developed. This coil is used to shift the frequencies of the trapped electrons, thereby matching them to the cavity modes generated by the trap electrodes. The simulation shows that a two-coil geometry is the best option to achieve a strong and homogeneous magnetic field within the given boundary conditions of the experiment. Additionally, several methods for spot welding joints between NbTi wires are tested. No significant difference between a direct joint and a joint performed within a NbTi cylinder is observed. Furthermore, the wire diameter has no significant influence on the achievable current, which is determined to be over 2.5 A for a 0.5 mm wire diameter and over 1.4 A for a 0.3 mm wire diameter in a zero background field. Higher currents were not investigated. In an initial test using a 7 T background field, the tested joint lost its superconductivity for reasons that could not be futher investigated due to time limitations. The other joints were not tested in the strong background field.

Zusammenfassung

Die zunehmende Präzision von Penning-Fallen-Experimenten erfordert die Entwicklung neuer Kühlungstechniken, um Teilchen in ihren Grundzustand zu kühlen. Ein vielversprechender Ansatz für Ionen, die nicht lasergekühlt werden können, ist die sympathetische Kühlung mithilfe einer selbstgekühlten Elektronenwolke. Dieser Ansatz wird aktuell im ELCOTRAP-Experiment am *Max-Planck-Institut für Kernphysik* (MPIK) untersucht.
In dieser Arbeit wird eine supraleitende B_0-Justierungsspule für ELCOTRAP entwickelt. Diese wird genutzt, um die Frequenzen der gespeicherten Elektronen in Resonanz mit den Moden des Hohlraumresonators, der von den Fallenelektroden gebildet wird, zu bringen. Die durchgeführten Simulationen zeigen, dass eine Konfiguration aus zwei Spulen am besten geeignet ist, um ein starkes und homogenes Magnetfeld innerhalb der Falle zu erzeugen. Außerdem werden verschiedene Methoden getestet, um die NbTi-Spule mit dem Punktschweiß-Verfahren supraleitend zu verbinden. Dabei zeigt sich, dass es keinen signifikanten Unterschied macht, ob die Drähte direkt miteinander oder in einer NbTi-Hülse verschweißt werden. Auch der Drahtdurchmesser hat keinen entscheidenden Einfluss auf den erreichbaren Strom der Verbindungen. Ohne Hintergrundfeld wurde für einen Drahtdurchmesser von 0.3 mm ein kritischer Strom I_C von mindestens 1.4 A gemessen, während für einen Durchmesser von 0.5 mm I_C über 2.5 A lag. Höhere Ströme wurden in dieser Arbeit nicht getestet. In einem ersten Test in einem Hintergrundfeld von 7 T war der getestete Joint nicht supraleitend. Die Gründe hierfür konnten aufgrund von mangelnder Zeit nicht weiter untersucht werden. Die anderen Joints wurden nicht in diesem Hintergrundfeld getestet.

Contents

List of Figures

List of Tables

Chapter 1

Introduction

The Standard Model of particle physics is one of the great successes of modern physics. It describes the most fundamental particles and their interactions, and some of its predictions have been tested to a relative precision of 10^{-12} [1]. Central to this context are the masses of single particles and their magnetic moments, i.e. g-factors, with precise measurements of both being key ingredients for the most stringent tests of the Standard Model, including tests of CPT symmetry [2] and quantum electrodynamics [1].

The CPT symmetry is of interest, as it challenges a crucial aspect of the Standard Model. According to theory, one would expect equal amounts of matter and antimatter to exist [3]. However, in the observable universe, ordinary matter far outweighs antimatter, indicating that there may be a subtle difference between the two. To verify or disprove this, the mentioned measurements of the charge-to-mass ratios or g-factor ratios of e.g. the proton and the antiproton are necessary. Moreover, exact mass measurements are required in various fields, such as chemistry (requiring a relative mass precision of $\delta m/m \leq 10^{-5}$), astrophysics ($\leq 10^{-7}$), and atomic physics ($\leq 10^{-11}$) [4].

Today, mass measurements and the determination of g-factors are performed using Penning traps. For the operation of Penning traps, proper cooling of the particles is essential, as cooling reduces the motional amplitudes of stored particles, thereby minimizing the influence of field imperfections inside the trap [4]. Additionally, cooling decreases relativistic shifts, and the particles occupy a smaller thermal phase space [5]. Since these effects inhibit more precise measurements, effective cooling is crucial for the development of high-precision Penning-trap experiments. The evolution of precision in Penning traps drives the need for new, even-better, cooling techniques and the ELCOTRAP experiment is exclusively dedicated to develop and test new cooling techniques.

The ELCOTRAP experiment is a Penning-trap experiment based at the *Max Planck Institute for Nuclear Physics* (MPIK) that investigates sympathetic cooling of ions using electrons. In this technique, a stored ion is coupled to a well-cooled electron cloud via image

currents, allowing the ion to transfer energy to the electron cloud. The electron cloud, that is in equilibrium with the ambient temperature of 4.2 K due to its cyclotron radiation, in turn cools the ion.
The electromagnetic cavity formed by the trap gives raise to certain cavity modes and to realize the coupling and an effective cooling by cyclotron radiation, a fine-tuning of the electron oscillation present in the trap and the available cavity modes must be achieved.
In this work, a superconducting tuning coil is developed, which is designed to create a magnetic field in the trap that can be used to shift the frequencies within the trap and thus, match them to the cavity modes. The development process includes simulating the optimal geometry for the coil to achieve the highest possible magnetic field strength and investigating different methods for joining the coil. Although many techniques are presented in the literature, none of the techniques for joining thin wires have been systematically tested in a high background field. Therefore, an investigation of gas tungsten arc welding joints within the 7 T magnet of the ELCOTRAP experiment are performed. Additionally, a coil simulation for a B_2-coil for temperature measurements in Penning traps is conducted and is presented.

The next chapter provides the theoretical background for this work. Chapter 3 introduces the ELCOTRAP experiment, followed by a presentation of the coil geometry simulations in chapter 4. Chapter 5 discusses the results of the performance measurements for different joint methods and outlines how superconducting joints can be performed and tested. In chapter 6, the joints are tested in a strong background field of 7 T. Finally, chapter 7 describes the manufacturing and implementation of the tuning coil in the ELCOTRAP experiment.

Chapter 2

Theoretical basics

In the following chapter, the theoretical foundations of this thesis will be presented. This includes an introduction to Penning traps, methods for measuring the temperature of a single trapped particle, and a brief overview of superconductors and joints. Additionally, the basics of magnetic fields and coils are introduced.

2.1 Penning traps

Penning traps are one of many possible designs for trapping particles and are used in a variety of fields, such as mass measurements [6, 7, 8, 9] or measurements of the magnetic moment [10, 11]. Due to Earnshaw's theorem [12], a charged particle cannot be held in stable equilibrium in either a pure electrostatic or a pure magnetostatic field. Therefore, a Penning trap combines electrostatic and magnetostatic fields, which then allows for the storage of charged particles.

2.1.1 The ideal Penning trap

The operation principle of a Penning trap is based on a homogeneous magnetic field $\vec{B} = B_0\vec{e_z}$ with field strength B_0, which was arbitrarily chosen to point into the z-direction of the trap. This leads to a Lorentz force $\vec{F_L} = q\left(\vec{v} \times \vec{B}\right)$, that forces a particle with charge q moving perpendicular to $\vec{B}$ into a circular orbit in the radial (x/y) plane. The frequency of this motion is given as

$$\omega_c = \frac{q}{m} B_0, \tag{2.1}$$

where m is the particle's mass. This frequency is called the cyclotron frequency, and the corresponding circular motion is known as cyclotron motion. However, the particle is still able to escape in the direction of the magnetic field. To prevent this, a second, electrostatic, field is applied. This field is created either by a geometry of hyperbolic or cylindrical elec-

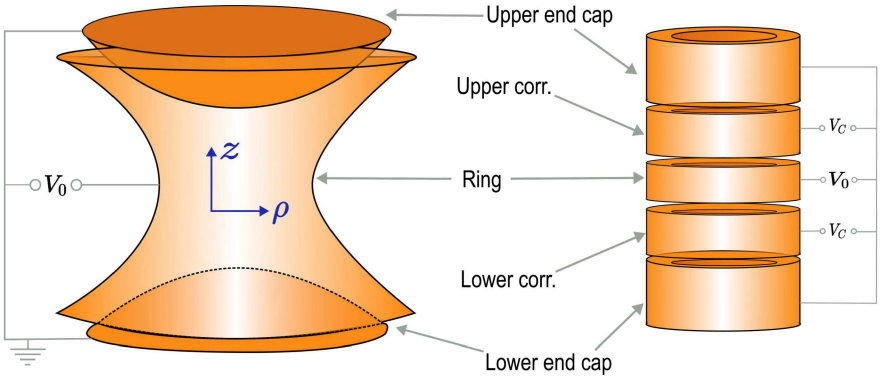

Figure 2.1: (Left) Penning trap with two end cap electrodes and one hyperbolic ring electrode. (Right) Cylindrical configuration to approximate the same potential in the center of the trap. For this purpose, at least two additional correction electrodes with an applied voltage V_C are needed.

trodes ([13], [14]), both configurations are shown in figure 2.1. In comparison, cylindrical electrodes are easier to manufacture and allow access along the z-axis, but require correction electrodes to create the requested potential. These correction electrodes are placed next to the end caps, and by applying the correct voltages to them, a tuning ratio can be found that approximates the potential of the hyperbolic geometry.
With a coefficient C_2 representing the geometry of the Penning trap and V_0 being the applied voltage between the electrodes, the ideal potential that is shown in figure 2.2 reads

$$\Phi(\vec{r}) = C_2 V_0 \left(z^2 - \frac{\rho^2}{2} \right) \tag{2.2}$$

and the corresponding fields are [4]

$$E_z = -\frac{\partial \Phi}{\partial z} = 2C_2 V_0 z \quad , \quad \vec{E}_\rho = C_2 V_0 \rho \vec{e_\rho}. \tag{2.3}$$

The combination of axial confinement from the electrostatic potential and radial confinement due to the Lorentz force now enables the trapping of particles, where the equation of motion (EOM) is now given by

$$m\ddot{\vec{a}} = q\left(\vec{E} + \vec{V} \times \vec{B}\right) = q\left(-\vec{\nabla}\Phi + \vec{v} \times \vec{B}\right) = qC_2 V_0 \begin{pmatrix} x \\ y \\ -2z \end{pmatrix} + qB_0 \begin{pmatrix} \dot{y} \\ -\dot{x} \\ 0 \end{pmatrix}. \tag{2.4}$$

For this EOM, the z-component can be readily solved and leads to a harmonic oscillator with axial frequency

$$\omega_z = \sqrt{\frac{2qC_2V_0}{m}}. \tag{2.5}$$

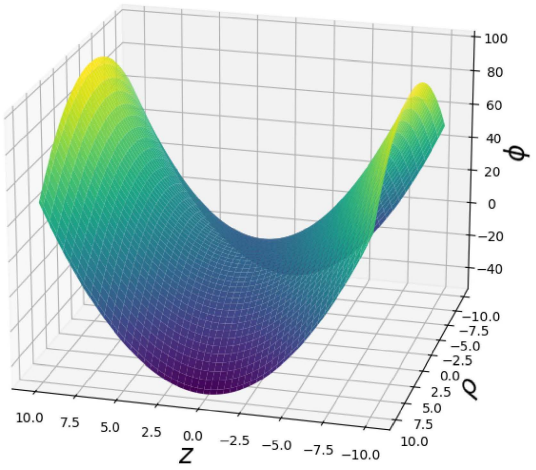

Figure 2.2: Electrostatic potential for axial confinement. One can see that the potential is confining in the z-direction, and therefore prevents the particles from escaping in that direction. In ρ-direction the potential is anti-confining and only the combination with the radial-confining Lorentz force enables the trapping.

To solve the remaining two coupled equations, one introduces the complex variable $u(t) = x(t) + iy(t)$ [15], resulting in harmonic oscillators with eigenfrequencies

$$\omega_- = \frac{\omega_c}{2} - \sqrt{\frac{\omega_c^2}{4} - \frac{\omega_z^2}{2}} \approx \frac{2C_2V_0}{B_0}, \tag{2.6}$$

$$\omega_+ = \frac{\omega_c}{2} + \sqrt{\frac{\omega_c^2}{4} - \frac{\omega_z^2}{2}} \approx \omega_c - \frac{2C_2V_0}{B_0}, \tag{2.7}$$

namely the magnetron (ω_-) and the modified cyclotron frequency (ω_+) [16].
Together, the three oscillators perform a combined motion shown in figure 2.3, where several relations hold between the individual motions. By demanding that the expression under the square root must remain positive, since only then a stable trapping is possible, a typical hierarchy emerges: $\omega_- \ll \omega_z \ll \omega_+ < \omega_c$. Combining equation (2.6) and equation (2.7), one sees that

$$\omega_- + \omega_+ = \omega_c, \tag{2.8}$$

but this equation only holds in ideal Penning traps. In real Penning traps, the Brown-Gabrielse-invariance theorem connects the single modes [17]

$$\omega_+^2 + \omega_-^2 + \omega_z^2 = \omega_c^2. \tag{2.9}$$

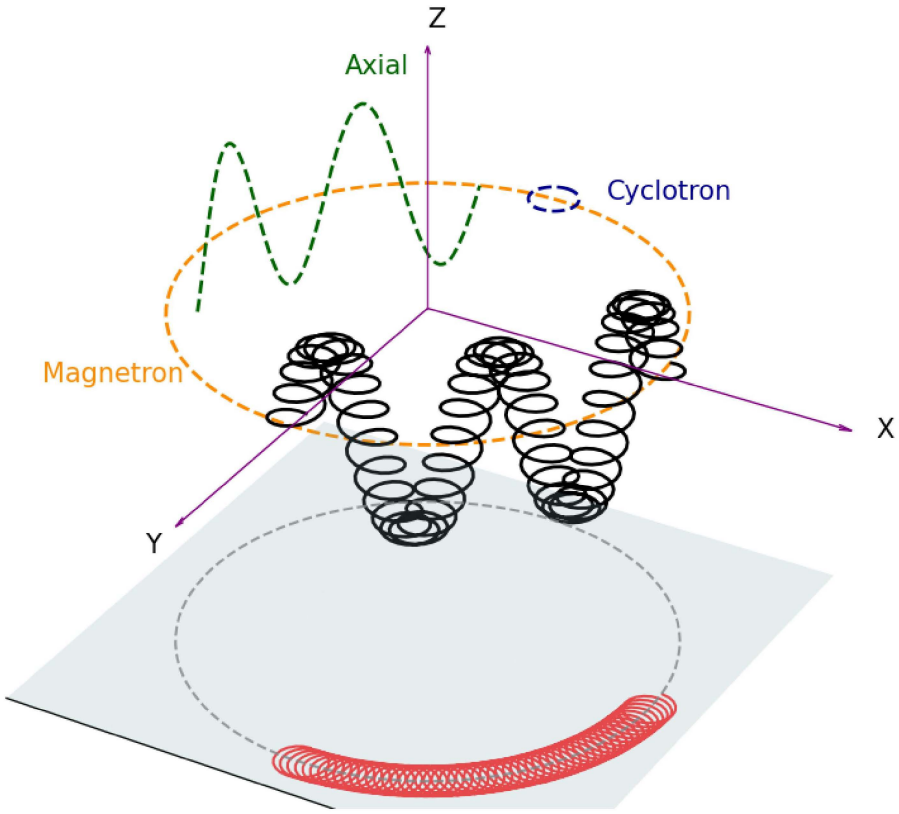

Figure 2.3: Combined motion in a Penning trap. The black line represents the real motion in the trap, created from a superposition of the three eigenmotions: The axial (ω_z), the magnetron (ω_-) and the modified cyclotron motion (ω_+).

By measuring the eigenfrequencies of the particle, for example with resonant electronic circuits described in section 2.1.5, and using this theorem, it is possible to determine the free cyclotron frequency, which is needed for mass or g-factor measurements.

2.1.2 The real Penning trap

In real Penning traps, several factors contribute to deviations from the ideal case, causing frequency offsets, energy-dependent frequency shifts, and coupling of the modes [18]. The main contributions are particle interactions, when more than one particle is present in the trap [4], misalignment between $\vec{E}$ and $\vec{B}$ as well as electric and magnetic field imperfections [19]. Since only magnetic field imperfections are relevant in this thesis, they are discussed below. Besides these effects, there are several other shifts resulting from relativistic shifts [5], field drifts [16] and image charge shifts [20], which will not be further discussed in the scope of this thesis. A theoretical treatment of these shifts can be found in [5] and [21].

Magnetic field imperfections: In a superconducting magnet, both temporal and spatial imperfections can occur, primarily due to inhomogeneities of the magnet itself and the magnetization of materials within the Penning trap [4, 19]. Temporal instability arises from factors such as temperature and pressure fluctuations, flux creep, or the influence of nearby ferromagnetic or paramagnetic materials [4]. Especially during measurements conducted over extended periods, such as testing the stability of a superconducting joint, these instabilities must be considered. On the other hand, spatial imperfections stem from sub-optimal shimming, which can be mitigated through improved shimming techniques.
All these imperfections lead to deviations from a homogeneous field and can be expressed in a power series along the z-axis around $z_0 = 0$,

$$B_z(z) = B_0 + B_1 z + B_2 z^2 + \dots . \tag{2.10}$$

The linear term does not affect the eigenfrequencies of the particle to first order, while the quadratic distortion results in a frequency shift that depends on the energy in the modified cyclotron motion E_+, given by [17]

$$\Delta\omega_z = \frac{E_+}{m\omega_z}\frac{B_2}{B_0}. \tag{2.11}$$

How this shift can be used to measure the temperature of a trapped particle is explained later on. An overview of other shifts present in the trap can be found in [22].

2.1.3 Coupling of the modes

Coupling the individual modes to cool particles in a Penning trap is a crucial technique, that will be explained in the following section. Additionally, manipulating the eigenmotions of the particles is essential in this context and will also be introduced. To accomplish either a coupling or an excitation, a radio frequency (RF) signal is applied to the electrodes of the trap [22].

Dipolar excitation: Dipolar radiation can be used to excite individual modes. The irradiation of such a dipolar field with field strength E_0, a polarization vector $\hat{e}_i$, and with a non-zero component in the direction of the motion,

$$\vec{E}(t) = E_0 \sin(\omega t + \phi)\hat{e}_i \tag{2.12}$$

is realized by applying an appropriate sinusoidal RF voltage to the electrodes. The frequency ω must match one of the eigenfrequencies $\omega_{\pm,z}$ to excite the corresponding eigenmotion. For

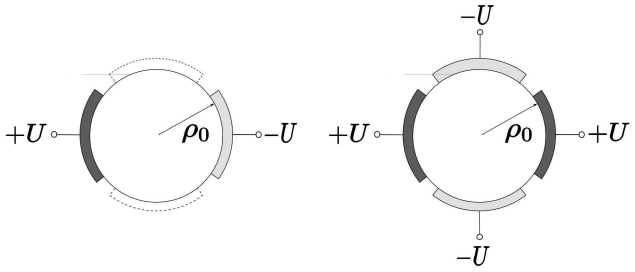

Figure 2.4: (Left) Two ring electrodes to irradiate a dipolar field by applying a voltage to opposite ring segments. (Right) A split electrode design is used to inject a quadrupole field by applying a radiofrequency signal between each pair of opposite segments in the four-fold segmented ring. This configuration allows for precise manipulation of the particle's motion within the trap by generating the desired quadrupole potential. (adapted from [4])

the excitation of the axial mode, a suitable dipolar excitation field is created by applying the RF voltage to the end cap electrodes, or, if present, to the correction electrodes. Manipulation of the radial motions is achieved with ring segment electrodes, as shown in figure 2.4. Increasing the amplitude of an individual motion can be used to eliminate unwanted ions by bursting them away.

Quadrupol excitation and coupling: Applying an RF voltage to one quadrant of a radially split electrode, as shown in figure 2.4, creates a quadrupolar field within the trap, that can be used to either purely couple specific eigenmotions of the particle or to couple the eigenmotions and excite them. To do so, a frequency matching the sideband, which is the sum or the difference of two eigenmotions, has to be chosen. In this case, a process analogous to Rabi oscillation occurs, and the actions of the eigenmotions are exchanged at half of the modified Rabi frequency [23],

$$\Omega = \sqrt{\Omega_0^2 + \delta^2}, \tag{2.13}$$

where δ is the detuning from the true sideband and Ω_0 is the Rabi-frquency in the Penning trap. For axial-radial coupling this frequency is given by

$$\Omega_0 = \frac{qE_0}{2m\sqrt{\omega_z \omega_\pm}}, \tag{2.14}$$

with E_0 being the field strength. A pure oscillation involves the transfer of energy back and forth between different motions. In this case, the two motions are in the same Landau level [24]. Whereas, coupling and excitation involve the transfer of energy between modes and the excitation of individual modes.

The applied field is given by

$$\vec{E}(t) = E_0 \sin(\omega_{\text{couple}} t + \phi)(x_i \vec{e_j} + x_j \vec{e_i}). \tag{2.15}$$

Depending on the choice of ω_{couple} one gets either a pure coupling or an excitation and coupling. In [22] and [25] an overview of the effects for different RF sidebands is given.
The realization of the coupling of the axial and modified cyclotron motion is one crucial part of ELCOTRAP, and the difficulties of that are outlined in section 3.2.

2.1.4 Temperature measurements in Penning traps

The first goal of this thesis is to develop a B_2-coil for temperature measurements within a Penning trap. This so-called magnetic bottle is one of many techniques to determine the temperature of a trapped particle. Following, a brief overview of additional methods for temperature measurement will be provided.
The first problem in this context is that temperature is usually only defined for large ensembles of particles. However, it is still possible to apply the concept of temperature to individual particles under certain conditions [26]. In Penning traps, the energy of the different motions is given by their amplitude ρ_i and frequency ω_i. If now the system is ergodic, meaning that a time average and an ensemble average are the same, the temperature can be determined by a consecutive measurement of the energy over a certain time interval [26]. This is the case when the system is in thermal equilibrium with a heat bath. For example, the detection electronics for ions or black-body radiation for electrons are such heat baths.
Two other ways for a temperature measurement are outlined in [26], where the temperature of an ion attached to the detection electronics can be obtained by measuring the noise of the electronics and in [27], where the "Fluorescence Lineshape" is presented.
However, the most common way for temperature measurements is with magnetic bottles, as described in [22] or [26]. A magnetic bottle involves a B_2-field in the Penning trap. The energy associated with the modified cyclotron motion is directly related to this field via equation (2.11).
So if B_0 is known and the axial frequency ω_z is measured, the energy can be obtained by introducing the particle into a B_2-field of known strength and measuring ω_z again. In this way, the cyclotron temperature can be obtained. To determine the axial temperature, one has to couple the axial to the modified cyclotron motion. Due to the coupling, both oscillations have the same quantum number [22] and therefore the energies are related via

$$\frac{E_+}{\omega_+} = \frac{E_z}{\omega_z}. \tag{2.16}$$

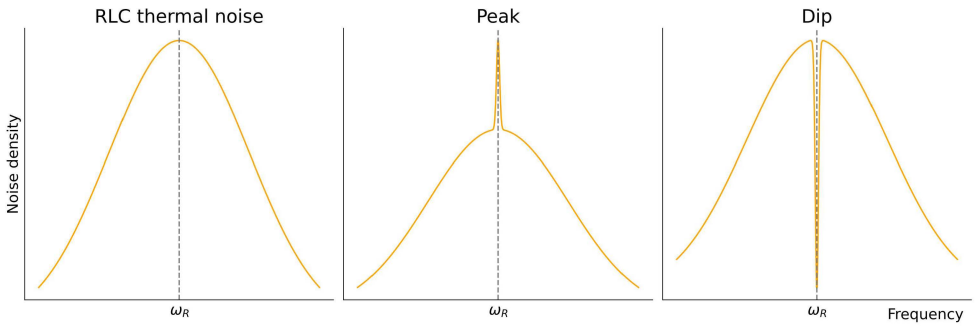

Figure 2.5: Sketch of recorded signals during the particle detection. (Left) Recorded noise of the resonator without a particle. The maximum is at the resonance frequency of the circuit. (Middle) Uncooled ("hot") particle in the trap. If the particle's frequency is in resonance with the resonator's resonance frequency, it appears as a peak according to equation (2.20). (Right) A particle in equilibrium with the resonator ("cold" particle) can be modeled as a short, and therefore creates a dip in the noise spectrum. (adapted from [22])

So the axial temperature is

$$T_z = \frac{\langle E_z \rangle}{k_B} = \frac{\langle E_+ \rangle}{k_B} \frac{\omega_z}{\omega_+}. \tag{2.17}$$

The drawback of this method is that most applications require a highly homogeneous magnetic field, which conflicts with the presence of B_2-inhomogeneity.

2.1.5 Particle detection in Penning traps

To test the produced joints within a strong background field, they must be placed inside the magnet of the ELCOTRAP experiment. This magnetic field is approximately 7 T, making conventional magnetic sensors ineffective in this environment. However, the joints can be tested using a stored ion and measuring frequency shifts in its motions. For this, a coil, containing the joint to be tested, is wrapped around the trap chamber, creating an additional B-field. If the joint enables a persistent mode, the frequency of the trapped particle should shift compared to the case without the test coil. This shift should be, within the scope of measurement accuracy, constant. To measure this shift, the *Fourier Transform Ion Cyclotron Resonance* (FT-ICR) technique is used. The following description of this method is based on [23], [28] and [29].

Induced image current: A particle with charge q performing a harmonic oscillation along the z-axis with frequency ω_z and amplitude Z_0 induces an image current

$$I_{\text{ind}} = \frac{qZ_0\omega_z}{D_{\text{eff}}} \sin(\omega_z t) \tag{2.18}$$

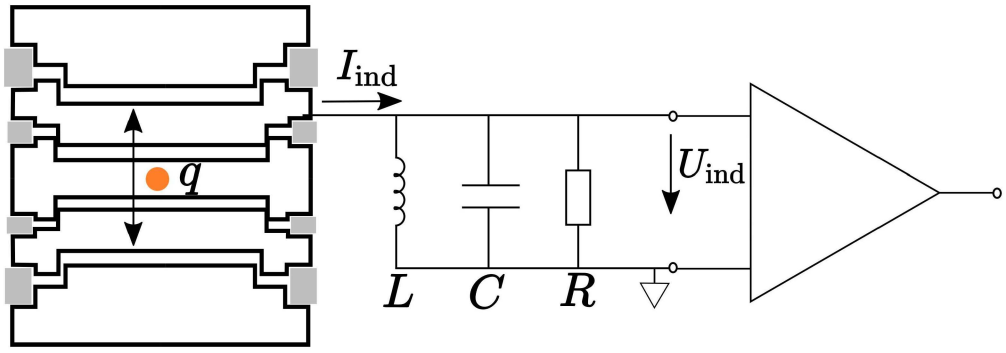

Figure 2.6: Detection circuit for frequency measurements within Penning traps. The resonator consists of an inductor L connected to the electrodes of the Penning trap, the parasitic capacitance of the trap C and a resistor R made up by the Ohmic losses. Next to the circuit is an amplifier connected.

in the electrodes of the Penning trap [30]. Here, D_{eff} is the effective electrode distance, for which a value is derived in [23]. Unfortunately, these currents are on the order of a few femtoamperes (fA), and therefore, too small to be measured directly.

LCR-circuit: However, these small currents can be amplified using an LCR circuit and a cryogenic amplifier. The LCR-circuit can be created by connecting an inductor with inductance L to the electrodes. Together with the parasitic capacitance of the trap and the Ohmic losses, which can be modeled as a resistor R, the LCR circuit is formed. A sketch of this setup is shown in figure 2.6.
The voltage drop across this circuit is directly related to the impedance of the circuit, given by

$$Z_{\text{LCR}}(\omega) = (R^{-1} + (i\omega L)^{-1} + i\omega C)^{-1} \tag{2.19}$$

$$\longrightarrow U_{\text{ind}}(\omega) = I \cdot \omega L \left(\frac{1}{\frac{1}{Q} - i\left(1 - \frac{\omega^2}{\omega_{LCR}^2}\right)} \right), \tag{2.20}$$

where $\omega_{\text{LCR}} = (LC)^{-1/2}$ is the resonance frequency and $Q = R/(\omega_{\text{LCR}} L)$ is the quality factor. The maximum voltage occurs when the particle's frequency ω matches the resonance frequency of the circuit, leaving only the real valued impedance R. To match the two frequencies, the trap potential V_0 in equation (2.5) can be varied, adjusting ω_z to the resonance frequency.

Detector feedback: At resonance, the voltage drop across the resonator produces an additional electric field inside the trap. This creates a counteracting force that damps the

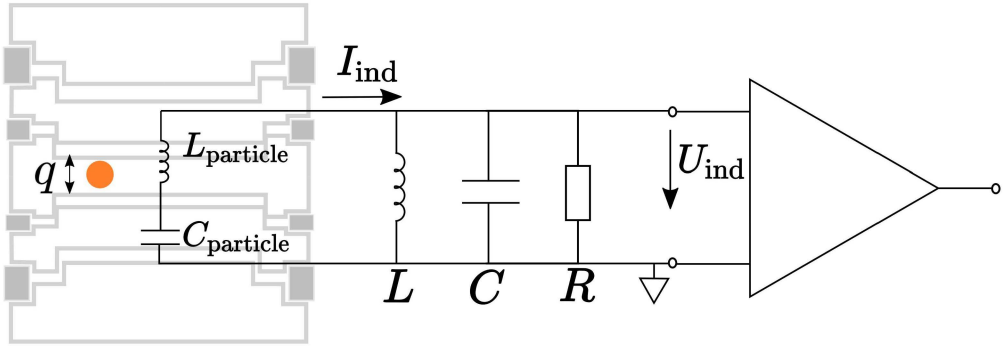

Figure 2.7: Equivalent circuit for a particle in thermal equilibrium with the resonator. In this case, the particle can be modeled as a tank circuit with capacity L_{particle} and inductance C_{particle}.

particle's oscillation. For the z-direction, the force reads

$$F = -Eq = -\frac{q}{D_{\text{eff}}} U_{\text{ind}} = -\frac{q^2 Z_{\text{LCR}}}{D_{\text{eff}}^2} \dot{z}, \tag{2.21}$$

and must be included in the EOM (2.4). The solution is $z = Z_0 e^{\lambda t}$, where λ is given by

$$\lambda = -\frac{\Gamma}{2} + i\omega_z \sqrt{1 - \frac{\Gamma^2}{4\omega_z^2}}, \tag{2.22}$$

with the damping factor $\Gamma = \frac{q^2 Z_{\text{LCR}}}{m D_{\text{eff}}^2}$.
This damping allows energy to be transferred from the axial motion to the resonator until an equilibrium between damping and driving from the noise of the resonator is reached. This method is known as resistive cooling, and a more detailed treatment can be found in [23] and [28]. By coupling different motions, this technique can also be used to cool other motions besides the axial motion.

Equivalent circuit: Once the ion and the resonator reach the equilibrium temperature, the ion can be modeled as a tank circuit [31], with

$$L_{\text{particle}} = \frac{m D_{\text{eff}^2}}{q^2} \quad \text{and} \quad C_{\text{particle}} = \frac{q^2}{m\omega_z^2 D_{\text{eff}^2}}. \tag{2.23}$$

A schematic of the equivalent circuit is shown in figure 2.7. This LC-circuit acts as a short when approaching ω_z, leading to a dip in the resonator's noise spectrum. This dip allows for the detection of the ion's motion by fitting an appropriate physical model to the dip, and an example of such a dip is shown in figure 2.5. The width of this dip can be used to determine the number of trapped particles [23], and it has a Lorentzian lineshape [28].

Table 2.1: Properties of some superconductors. The uncertainty in NbTi and Nb_3Sn is due to different alloy ratios. All values taken from [36].

Material	T_C / K	B_C / T
Pb	7.196	0.08
Al	1.175	0.01
Nb_3Sn	≈ 18	$\approx 23 - 29$
NbTi	≈ 10	$\approx 10 - 13$

2.2 Superconductors

2.2.1 Basic properties

In cryogenic experiments, using superconducting coils is essential, as even the best conventional conductors would result in high Ohmic dissipation and significant heating.
Superconductivity is a phenomena discovered back in 1911 [32], describing the properties of certain materials below a critical temperature T_C. Below this threshold, the electrical resistance of superconductors vanishes and the magnetic field is expelled from the material [33], meaning that superconductors are perfect electric conductors and ideal diamagnets. Besides the critical temperature, the critical magnetic field B_C and the critical current density j_C are important quantities of superconductors. B_C represents the critical magnetic field strength at which a superconductor transitions to a normal conducting state, while j_C denotes the critical current density at which this transition occurs [33].
Superconductors are classified into type I and type II. While type I superconductors are typically pure metals, like lead or mercury, that completely expel magnetic fields until the critical value B_C is reached, type II superconductors [34], such as alloys like niobium–titanium (NbTi), exhibit an intermediate phase where both ordinary and superconducting phase coexist. Table 2.1 lists some examples of the critical magnetic fields and critical temperatures for different superconductors. To verify if a material is superconducting, one can use either the Meißner-Ochsenfeld effect [35] or measure the magnetic field created by a superconducting coil, as this field should remain constant due to the lack of losses. Once a current is injected in a closed loop, the current in the loop should remain constant over time even after the power supply is turned off and hence, this operation state is named persistent current mode.
Most type I superconductors have a too low critical B-field for our operational needs, so an alloy is required. For example, NbTi is a suitable material for our operations in a 7 T field, as shown in table 2.1. Compared to Nb_3Sn, NbTi is more mechanically deformable and therefore better suited for the production of a coil. According to [37], NbTi also has an excellent critical current density j_C of over $1\,\mathrm{kA/mm^2}$. Most superconducting wires are manufactured by placing the superconducting strand within a surrounding matrix. A schematic of the cross-section of such a wire is shown in figure 2.8. The insulation ensures

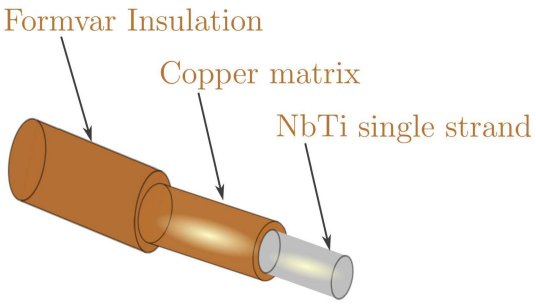

Figure 2.8: Cross-section of a superconducting wire. The NbTi strand is surrounded by a copper matrix and a formvar insulation.

that no shorts appear, while the copper matrix provides good thermal coupling and gives mechanical strength, stabilization, and protection.

2.2.2 Joints between superconductors

For a persistent current mode operation, the two ends of the wire must be connected with a joint, such that the joining area is also superconducting and stays superconducting in a background field of 7 T. Additionally, the joint should have a high critical current density to maximize the critical current, thereby ensuring a strong magnetic field.
Superconductors have a broad range of applications, leading to the development of many techniques for creating joints, as reviewed in [38]. The following two examples could be used with the facilities at the MPIK.
The first method is the solder matrix replacement [39, 40]. The advantage of this is its easy handling. However, the problem with this technique is the low critical B-field of the solders. Depending on the exact composition, the critical field can reach only up to $\sim 2\,\mathrm{T}$ [39, 41].
Another method, described in [42], is cold pressing. In this technique, the strains are pressed together with a high pressure to bring them close together. Once the distance between the two components is only a few Angström, the electrons of both are shared, resulting in a bond, and therefore in a weld. Unfortunately, there is very little research regarding the properties of cold-pressed joints, particularly for operation in high background fields. Other techniques include electromagnetic forming [43], resistive welding [44], and supersonic welding [45].
For this work, the method of spot welding [46] was chosen because all the necessary tools for this procedure were available, and it demonstrated good results in previous experiments, for example in reference [47]. In this method, the two single strands are spot welded using an argon-ion arc-discharge spot welder (Lampert, PUK-5), thereby creating the superconducting joint. The steps are:

1. Removing insulation mechanically
2. Etching the copper matrix with nitric acid
3. Cleaning bare filaments with ethanol and water

4. Twisting filaments and performing the weld

The difficulties and specific settings are explained in chapter 5.

2.3 Magnetic fields and coils

The magnetic field generated by a steady electric current can be calculated using the Biot-Savart law [48],

$$\begin{aligned} d\vec{B}(\vec{r}) &= \frac{\mu_0}{4\pi} I d\vec{l} \times \frac{\vec{r} - \vec{r'}}{|\vec{r} - \vec{r'}|^3} \\ \leftrightarrow \vec{B}(\vec{r}) &= \frac{\mu_0}{4\pi} \int_V \vec{j}(\vec{r'}) \times \frac{\vec{r} - \vec{r'}}{|\vec{r} - \vec{r'}|^3} dV', \end{aligned} \tag{2.24}$$

where $\vec{j}$ is the current density and $\vec{r'}$ is the position of the conductor. For a single loop with radius R along the z-axis, the magnetic field along the z-axis is given by

$$B_z(z) = \frac{\mu_0 I}{2} \frac{R^2}{(R^2 + z^2)^{3/2}}. \tag{2.25}$$

Starting from this equation, the field of a coil can be approximated as a superposition of the fields from multiple loops placed along an axis. If the expansion of the coil is small compared to the distance at which the field is evaluated, a good approximation is

$$B_{z,\text{tot}} = B_z(z) = \frac{N \mu_0 I}{2} \frac{R^2}{(R^2 + z^2)^{3/2}}, \tag{2.26}$$

where N is the number of windings.
Given that formula, different geometries for special requests can be found. For a homogeneous magnetic field, which is required for a constant frequency shift within the trap, the most common choice is the Helmholtz coil. In this configuration, two coils of radii R are placed at a distance $d = R$, because at this distance the second derivative of equation (2.25), B_2, vanishes, making the field homogeneous. The first derivative vanishes anyway due to symmetry. However, other designs with more coils are possible for generating higher-order homogeneities. In general, with n pairs of coils $(2n - 1)$ derivatives can be set to zero, because that is the number of free variables [49]. For example, with two pairs of coils, there are three parameters u_1, u_2 that are the ratios of the diameter of the coils and their distance and the ratio of the coil radii $\rho = R_1/R_2$. Some possible configurations are shown in figure 2.9 and the ratios are presented in table 2.2.
The problem with these configurations is the approximation in equation (2.26). This is not valid for our given setup with dimensions on the order of $R_{\text{coil}} \approx 15\,\text{mm}$, coil thickness

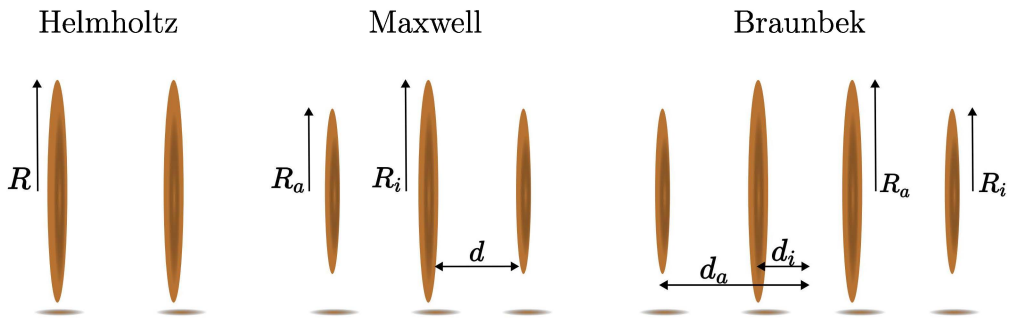

Figure 2.9: Overview of some possible configurations to create a homogeneous magnetic field

$t \approx 5\,\text{mm}$, and coil distances $d \approx 15\,\text{mm}$. Consequently, the B-field has to be calculated as a superposition of equation (2.25). This term does not have a calculable solution for vanishing derivatives, thus the best configuration has to be found using an optimizer. The concrete steps are presented in chapter 4.

Table 2.2: Overview of ratios for different configurations to create homogeneous magnetic fields.

Name	# Coils	Ratios	Reference
Helmholtz	2	$R = \text{d}$	
Maxwell	3	$R_a = (4/7)^{1/2} R_i$ $d = (3/7)^{1/2} R_i$ $I_i = 64/49 I_a$	[50]
Braunbek	4	$\rho = R_i/R_a = 1.309$ $d_a/R_a = 1.107$ $d_i/R_i = 0.278$	[49]

Chapter 3

The ELCOTRAP experiment

The ELCOTRAP (Electron Cooling Trap) is a Penning-trap experiment at the MPIK designed to investigate a novel cooling technique for Penning traps, as the increasing precision within Penning-trap experiments drives the need for new methods to reach temperatures near 0 K. As outlined in chapter 1, a sufficient cooling is necessary to reduce the uncertainties in the measurements and increase the accuracy of Penning-trap measurements. There are several cooling methods used in other Penning-trap experiments, like laser cooling [51], buffer gas cooling [52, 53], resistive cooling [54, 55] or evaporative cooling [56]. Below, the for this thesis relevant components and the basic idea of ELCOTRAP are presented.
In the ELCOTRAP experiment, particles are cooled using an electron cloud. The primary focus of this setup is not on achieving the highest possible precision, but on testing the principle of sympathetic cooling of ions with cold electrons. To facilitate this, a design, shown in figure 3.1, has been chosen that allows for rapid iteration cycles. The entire setup is enclosed within a 7 T magnet, in which the Penning trap and electronics are housed. Thanks to the horizontal bore, the experiment can be easily inserted into or extracted from the magnet using linear rails. Additionally, the entire setup can be cooled down to 4 K in less than 12 hours, further enabling quick iteration cycles.

3.1 Sympathetic cooling of ions via cold electrons

In the ELCOTRAP setup, two Penning traps are positioned adjacent to each other. The first trap confines an electron cloud, while the second trap stores the ion that is to be cooled. Since the axial eigenfrequency ω_z of a stored electron in a Penning trap is in the same order of magnitude as the cyclotron frequency ω_+ of an ion in a Penning trap, the two species can be coupled, enabling sympathetic cooling of the ion by the electrons. The exact frequencies of ELCOTRAP for a specific applied voltage are shown in table 3.1.
The self-cooling of the electrons is caused by their emission of cyclotron radiation.

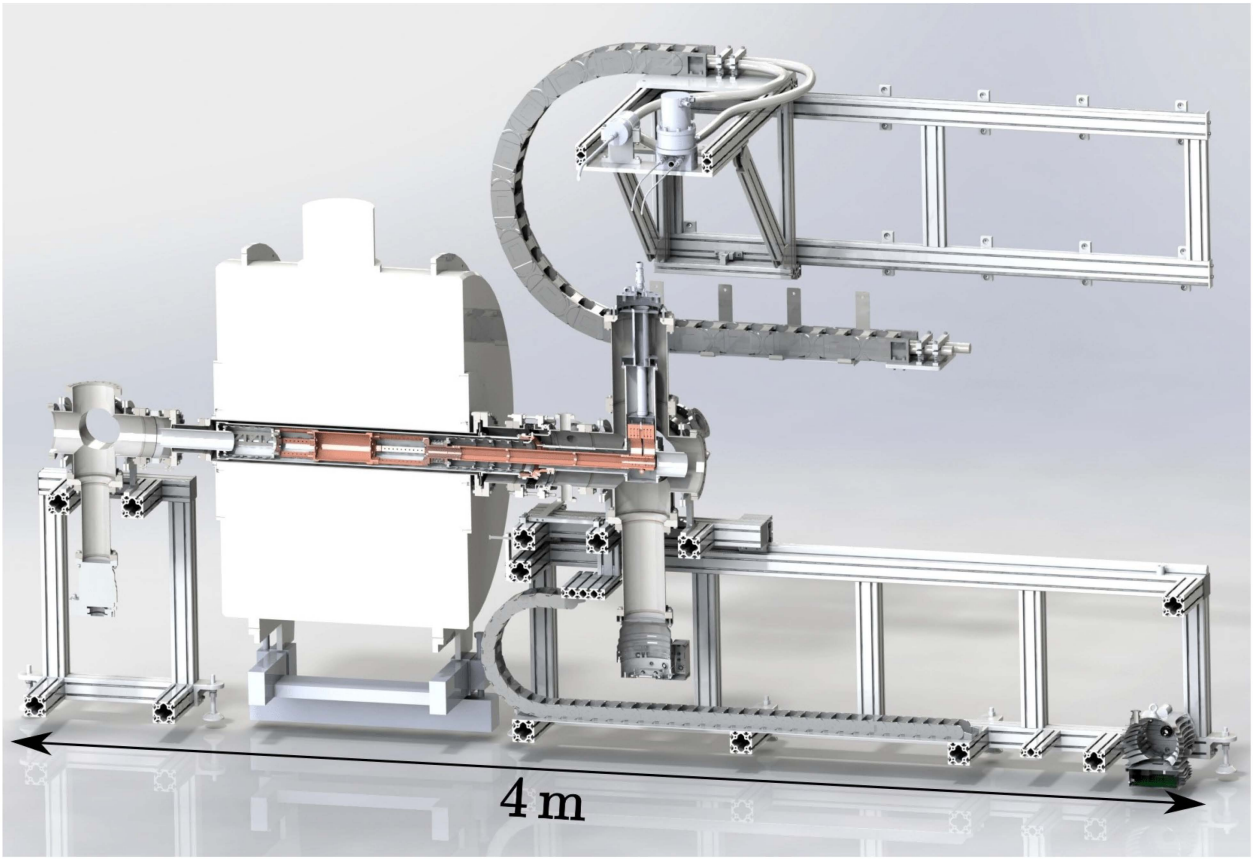

Figure 3.1: Setup of the ELCOTRAP experiment. In the center one can see the trap chamber mounted on a rail system allowing fast iteration cycles. The whole setup is cooled to 4.2 K.

This radiative cooling leads to a power dissipation [57]

$$P = -\frac{dE}{dt} = \frac{\sigma_t B^2 v^2}{c\mu_0}, \tag{3.1}$$

where σ_t is the Thomson cross-section, B is the applied field and v the particle's velocity. The cooling rate for the cyclotron motion is

$$\gamma_+ = \frac{e^2\omega_+^2}{3\pi\epsilon_0 m_e c^3}, \tag{3.2}$$

corresponding to a cooling time of $\tau_+ = 2\pi/\gamma = 331\,\text{ms}$. Via this cooling, the electron's cyclotron motion can cool down to the ambient temperature, which is ideally 4.2 K. This cooling rate can further be enhanced using the Purcell effect [58] and as a result, the modified cyclotron motion is rapidly well cooled to $\approx 4.2\,\text{K}$. Using the coupling introduced in section 2.1.3 the axial motion can now be cooled to the same quantum state by coupling the axial mode to the cyclotron mode with an RF field. Assuming the axial mode is cooled to 4.2 K, it can be coupled to the ion's cyclotron motion in the other Penning trap through an

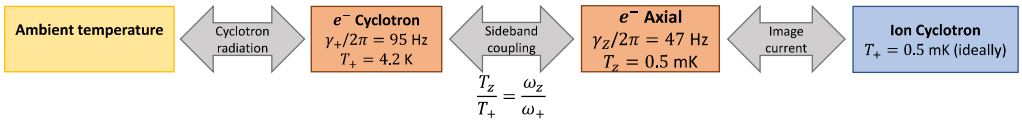

Figure 3.2: Flow chart of the couplings in the ELCOTRAP experiment. Each arrow indicates that the two boxes left and right are in equilibrium due to the process mentioned in the arrow.

Table 3.1: Frequencies in the ELCOTRAP setup. The applied voltage at the electron trap is here $U_0 = 5.6\,\mathrm{V}$ and $U_0 = -7.5\,\mathrm{V}$ at the ion trap.

	ω_z / Hz	ω_+ / Hz	ω_- / Hz
Electron trap	$2\pi \cdot 27.32 \cdot 10^6$	$2\pi \cdot 197.48 \cdot 10^9$	$2\pi \cdot 1890.01$
Ion trap	$2\pi \cdot 523.33 \cdot 10^3$	$2\pi \cdot 54.18 \cdot 10^6$	$2\pi \cdot 2527.55$

image current. For this, an electrical connection between an axial-sensitive electrode of the electron trap (ET) and a cyclotron-sensitive electrode of the ion trap (IT) is realized. This could for example mean to couple the end caps of the ET to a split ring electrode of the IT. As for the axial and the cyclotron motion of the electron, this means the ion's cyclotron motion is in the same Landau level [24] as the cyclotron motion of the electron. The full coupling scheme with the relevant values is shown in figure 3.2.

3.2 Coupling of the modes in ELCOTRAP

Looking at the coupling scheme in figure 3.2 and the frequencies in table 3.1, it is evident that the coupling between the axial and cyclotron frequencies of the electrons in the ET must be achieved using a sideband frequency in the order of 200 GHz. This corresponds to a wavelength of approximately 1.5 mm, which is smaller than the typical trap dimensions. Thus, the full electromagnetic wave picture must be considered when modeling the coupling field and the cyclotron radiation.

The electrodes of the Penning trap form an electromagnetic cavity, giving rise to specific cavity modes within the trap. These cavity modes are standing waves that either have a maximum or a node at the trap center [59]. Microwave cavities like these behave similarly to resonant circuits, meaning the cavity has certain resonant frequencies. If the cyclotron frequency is near resonance with a cavity mode, the spontaneous emission of cyclotron radiation is enhanced, allowing for faster cooling times to be achieved [60]. This is the Purcell effect mentioned in section 3.1. In addition to that, the sideband frequency must match a cavity mode to couple the axial and the modified cyclotron motion, thus achieving a

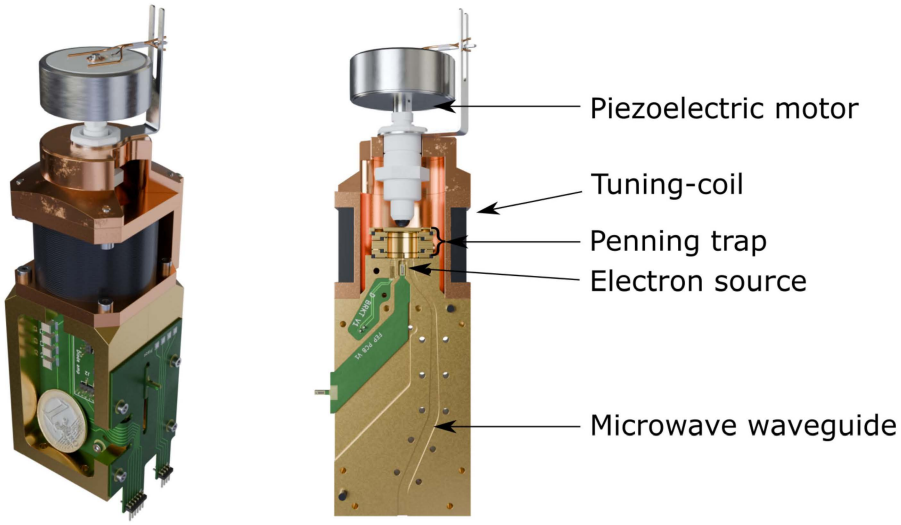

Figure 3.3: Design of the ET of ELCOTRAP. At the top of the setup, one can see the piezoelectric motor. Below located is the cylindrical Penning trap, which consists of a ring electrode, two correction electrodes and two end cap electrodes. One of the end cap electrodes also houses the microwave waveguide, used to inject microwaves into the trap. The trapped electrons are produced adjacent to the trap using an electron source.

sufficient axial cooling rate γ_z.

To accomplish that, the cavity modes in ELCOTRAP are adjusted using a piezoelectric motor, which can modify the trap dimensions and, consequently, the cavity modes. Furthermore, the cyclotron motion can be manipulated by altering the B-field according to equation (2.1). This B-field is generated by the superconducting tuning coil developed in this work. By fine-tuning both the sideband and cyclotron frequency to resonate with the cavity modes, sufficient cooling of the electron's axial mode can be achieved [17]. Finally, the now well-cooled axial mode of the electron can be coupled to the cyclotron mode of the ion.

3.3 Design of the electron trap

In the development process of the ELCOTRAP experiment, the first step is to design and manufacture the ET and check if proper cooling of the axial motion of the electrons can be achieved. Therefore, a design must be chosen that meets all the requirements to effectively couple the axial and cyclotron motions and achieve a sufficient cooling rate via cyclotron radiation. The design of the ET is shown in figure 3.3.

It consists of a piezoelectric motor that presses against one of the endcaps. In this way, the

trap dimensions, and thus the cavity modes present in the trap, can be adjusted. The piezo motor has a resolution of 5 nm and a travel range of 12 mm, though only a few hundred μm of this range are used. Below the piezo is the cylindrical Penning trap, which consists of five electrodes: one ring electrode, two correction electrodes, and two endcap electrodes. One of the endcap electrodes also houses the microwave waveguide, used to inject microwaves into the trap. These can be used to couple the modes of the trapped electrons. Surrounding the other four electrodes is the B_0-tuning coil developed in this work. As mentioned, this coil shifts the frequencies of the trapped electrons, thereby matching them to the cavity modes present in the trap. Finally, an electron source is placed below the trap. This source inject electrons into the trap by field electron emission.

Chapter 4

Simulation of coil geometries

For developing the superconducting tuning coil assembly and the B_2-coil assembly for temperature measurements, a suitable geometry has to be determined. Both assemblies consist of several coils, placed at appropriate distances. As outlined in section 2.3, the approximation of thin coils compared to their distance is not applicable in our case and therefore cannot be used. Additionally, as shown in figure 4.1, an approximation that considers only the edge windings is also inadequate. The difference between a calculation that includes all loops and one that accounts for only a few windings is significant. This is due to the magnetic field scaling as $\sim 1/r$. For a coil with a radius of approximately 10 mm and a wire diameter of 0.32 mm, the difference in the magnetic field between a wire at the edge and one $N = 5$ diameters placed away can be calculated as:

$$\Delta = \frac{1/10\,\mathrm{mm}}{1/(10\,\mathrm{mm} + N \cdot 0.32\,\mathrm{mm})} = \frac{11.6}{10} = 1.16$$

This means the B-field of an edge wire is 16 % higher than from a wire at the middle of the coil. Consequently, all windings must be taken into account in the design process.
Hence, the B-field is calculated as a superposition of individual loops. By summing all the individual loops, an analytical expression can theoretically be derived. However, this expression would be unmanageable long, especially considering the $\mathcal{O}(200)$ windings used for the coils. As a result, deriving an analytical solution by hand, or even with the aid of a computer, within a reasonable time frame becomes impractical. Therefore, the preferred approach is to optimize the configurations using a numerical algorithm. In this process, several variables can be adjusted:

- number of coils
- number of windings of each coil: N_a for outer coil, N_i for inner coil
- number of layers for each coil: L_a for outer coil, L_i for inner coil
- distance between coils: d_a for outer coil, d_i for inner coil

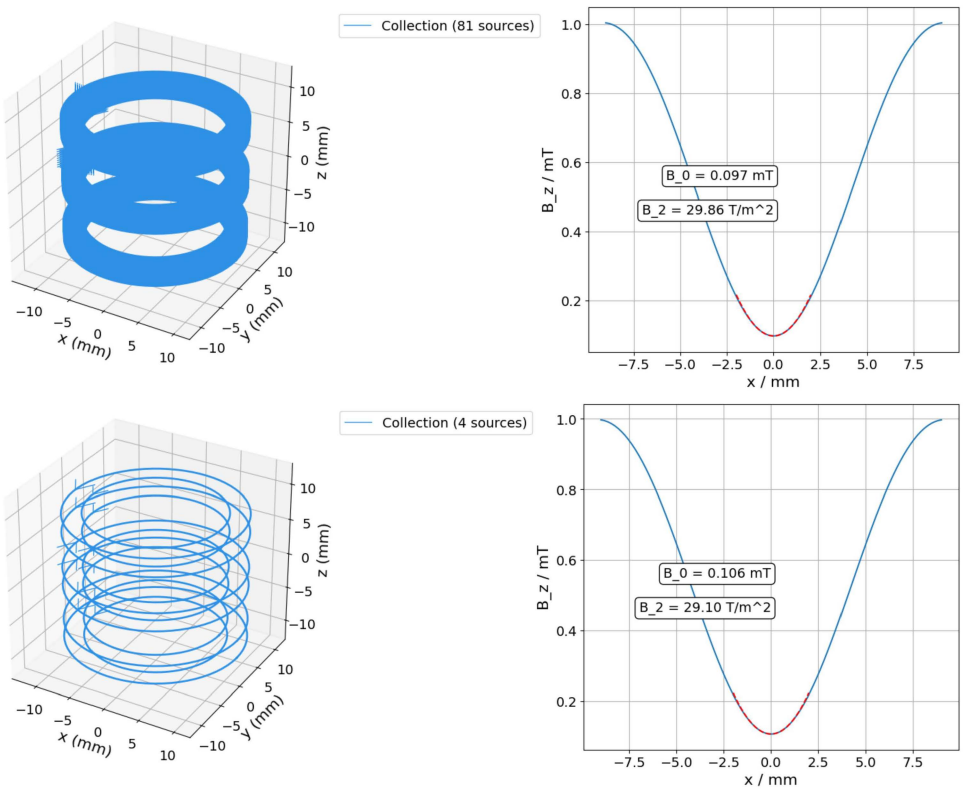

Figure 4.1: Comparison between a full configuration (top) and a configuration where only the edge windings, carrying 81/4 times the current, are considered (bottom). A significant difference of around 10 % between the two resulting B-fields is evident.

- radius of each coil: R_a for outer coil, R_i for inner coil

Some basic considerations help to restrict the parameters. Due to symmetry, the radii, number of layers and windings, and the spacing of the coils must be symmetric around 0. This is because both the tuning coil and the temperature coil should create an even B-field coefficient, specifically B_0 and B_2. As a result, the parameter space is reduced to between six and ten variables, depending on the assembly configuration, that can theoretically be adjusted. The number of coils, windings, and layers are discrete variables, while the others are continuous, leading to a mixed-integer problem. Additionally, the parameters must conform to the available space within the experiment and the individual coils should not overlap, which can be managed by applying specific constraints. Besides these constraints, it must also be considered that for the B_2- and B_0- coils, all other coefficients in equation (2.10) must be zero, resulting in an additional optimization constraint. The first three coefficients

evaluated at $z_0 = 0$ for a single loop are:

$$B_0 = \frac{\mu_0}{2}\left[\frac{R^2}{(R^2+z^2)^{3/2}}\right]$$
$$B_1 = \frac{\partial B}{\partial z} = -\frac{3\mu_0 I R^2}{2}\left[\frac{z}{(R^2+z^2)^{5/2}}\right]$$
$$B_2 = \frac{1}{2}\frac{\partial^2 B}{\partial z^2} = -\frac{3\mu_0 I R^2}{4}\left[\frac{R^2-4z^2}{(R^2+z^2)^{7/2}}\right].$$

These expressions include nonlinear terms in the optimization variables, making the optimization a mixed-integer nonlinear programming (MINLP) problem. To solve such problems, a variety of Python packages are available, such as GEKKO [61], Pyomo [62], and Gurobi [63]. However, these options are either restricted to commercial use or cannot handle constraints exceeding $\mathcal{O}(10,000)$ characters, which would be necessary for the superposition of $\mathcal{O}(200)$ windings. Consequently, using an MINLP solver is not feasible, and an alternative approach must be employed.
Therefore, in this work the optimization is done in the following way:

1. The coefficients of the magnetic field, B_0 and B_2, are calculated for all possible values of the integer variables $(N_a, N_i, L_a, \dots)$ that satisfy the boundary conditions imposed by the trap dimensions. This results in approximately $\mathcal{O}(10,000)$ to $\mathcal{O}(100,000)$ potential configurations. As a starting point for the following optimization, the continuous variables are set to their minimum values within the allowable range. For example, if the radius R of a coil could theoretically range from 10 mm to 15 mm, the calculations are performed using a radius of 10 mm.
2. For all configurations, B_0 or B_2 is maximized using SciPy [64]. To achieve this, the continuous variables are adjusted within the given boundary conditions. Additionally, other constraints, such as preventing coil overlap and ensuring the vanishing of the other coefficients, are applied.
3. From all configurations, those that successfully find a solution within the given boundary conditions are filtered out.

4.1 Coil for temperature measurement

The B_2-coil is intended to be used for temperature measurements in the ELCOTRAP experiment. Therefore, a high B_2 is necessary according to equation (2.17). This would correspond to a shift in the axial frequency, that can be measured with the method described in section 2.1.5.

Since the current I influences B_2 linearly, the specific value of the current only serves as a scaling factor and does not affect the optimal geometry. Therefore, all geometries are calculated with an arbitrary current of $I = 1\,\mathrm{A}$. Whether or not this current is realizable is investigated experimentally and is shown in chapter 5 and chapter 6. To generate a B_2-field without a B_0 component, there must be a symmetrical increase or decrease in the magnetic field along the z-axis, with the B-field vanishing at the center. This can be achieved by using an odd number of coils, where the innermost coil carries a current in the opposite direction to that of the outer coils.
To maximize B_2, the magnetic field's gradient should be as large as possible, meaning that from the zero field at the center a strong increase or decrease is necessary. Considering this, along with the space constraints in the actual experiment, it becomes clear that a configuration with 3 coils is an optimal choice for the B_2-coil. A configuration with 5 coils was also simulated, but the optimization resulted in the two outermost coils being effectively merged, forming a 3-coil configuration. Therefore, in the following discussion, only the case of a 3-coil configuration for the B_2-coil is presented.

Results: The parameters of a 3-coil system include the number of inner (N_i) and outer (N_a) windings, the number of layers (L_i, L_a), the radii (R_i, R_a), and the distance between the coils ($z_0 = d$), resulting in a total of 7 parameters. The trap dimensions constrain these parameters to $10.5\,\mathrm{mm} \leq R \leq 15\,\mathrm{mm}$ and $z_0 \leq 9\,\mathrm{mm}$. For all possible configurations within these boundaries, the magnetic field coefficients are calculated and optimized using the *scipy.minimize* function. This calculation is performed for two different wire diameters, and the results are as follows:

0.3 mm wire: $N_i = 25,\ L_i = 12,\ R_i = 10.55\,\mathrm{mm},\ N_a = 15,\ L_a = 14,\ R_a = 10.5\,\mathrm{mm},$
$z_0 = 9.0\,\mathrm{mm}$

0.5 mm wire: $N_i = 13,\ L_i = 8,\ R_i = 10.57\,\mathrm{mm},\ N_a = 9,\ L_a = 8,\ R_a = 10.5\,\mathrm{mm},$
$z_0 = 9.0\,\mathrm{mm}$

The corresponding frequency shifts of the axial particle motion for different currents can be obtained from equation (2.11) and are shown along with the generated B_2 in figure 4.2. The exact value of I will be tested in the following two chapters, but even with a very optimistic estimate of 2 A or 3 A, a frequency shift of only 7.45 Hz for a wire diameter of 0.3 mm and 6.66 Hz for a diameter of 0.5 mm can be achieved. According to [65] the dip width of the axial frequency in a measurement with the method described in section 2.1.5 is given as

$$\Delta\omega_z = \frac{R_{\mathrm{RLC}}}{m}\frac{q^2}{D_{\mathrm{eff}}^2}N, \tag{4.1}$$

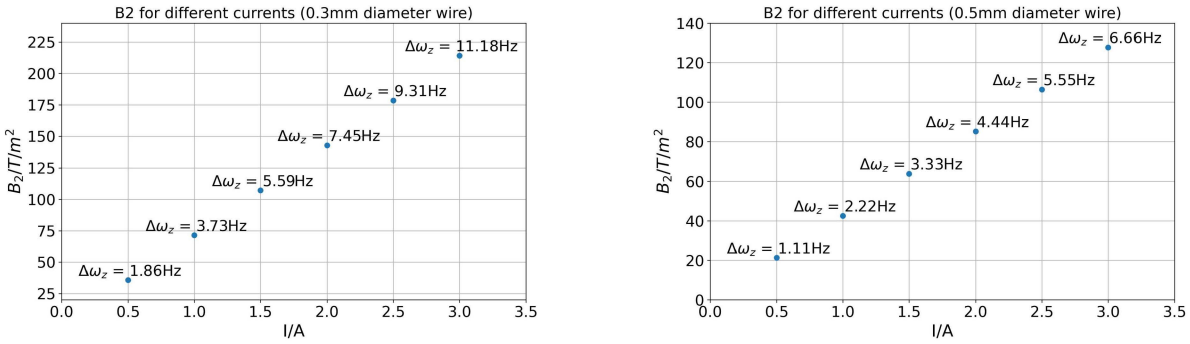

Figure 4.2: Maximum possible B_2 and the corresponding frequency shift for different values of I. (Left) result for a wire diameter of 0.3 mm, (right) result for a wire diameter of 0.5 mm.

where N is the number of trapped particles, R_{RLC} is the resistance of the detection circuit and D_{eff} the effective electrode distance introduced above. For the detection circuit in ELCOTRAP this dip width of a single electron is on the order of 10 Hz. Thus, the dip width is bigger than the shift from the B_2-coil, making a temperature measurement with this technique very difficult. Therefore, at the end, the B_2-coil was not included in the experiment. Nevertheless, it was demonstrated that the employed optimization algorithm is capable of optimizing complex coil geometries, which will become useful in future calculations.

4.2 Coil for frequency tuning

The second coil simulated in this work is designed to produce a homogeneous magnetic field. As described in chapter 3, this field is necessary to shift the cyclotron frequency and the axial-cyclotron sideband in the ET of ELCOTRAP to proper cavity modes.
For the coil assembly, various geometries and numbers of coils are possible. As outlined in section 2.3, none of the standard coil configurations (Maxwell, Braunbek, ...) are feasible, so a brute-force calculation is performed for different numbers of coils. In the experiment, the number of individual coils is imitated to between one and four coils due to the space constraint.
The boundary conditions for the design include a maximum height of 19 mm, corresponding to $z_0 = 9.5\,\text{mm}$, and a radius range of $12.26\,\text{mm} \leq R \leq 16.26\,\text{mm}$. Additionally, it is required that either B_2 alone or both B_2 and B_4 must vanish. Since the odd-order terms inherently vanish for symmetric assemblies, and higher-order terms do not significantly impact the frequency shift, they are neglected in the optimization.
The optimization process also reveals that the constraint $B_4 = 0$ is not always achievable and significantly affects the maximum reachable B_0. Given that the shift due to B_4 is 10^8

times smaller compared to the shift due to B_2, the optimization is focused on eliminating B_2 and disregards the value of B_4.
The optimization is performed using the algorithm presented in section 4.1, again for wire diameters of 0.3 mm and 0.5 mm, with *scipy*.

Results: A single coil performs poorly in creating a homogeneous B-field without higher-order B-field coefficients, so its results are not discussed here. Results for configurations with two, three, and four coils are presented again with a current of $I = 1\,\mathrm{A}$.
The results of the simulation for the 0.3 mm wire are shown in figure 4.3. There is only a small difference between the various numbers of coils, with the maximum achievable B-fields differing by less than 0.3 mT. The optimal configurations for the 0.3 mm wire are as follows:

$$\begin{aligned}
\textbf{Two coils:}\quad & N = 14,\ L = 12,\ R = 12.26\,\mathrm{mm},\ d = 7.18\,\mathrm{mm} \\
\textbf{Three coils:}\quad & N_i = 5,\ L_i = 1,\ R_i = 15.94\,\mathrm{mm},\ N_a = 14, \\
& L_a = 12,\ R_a = 12.26\,\mathrm{mm},\ d_a = 7.26\,\mathrm{mm} \\
\textbf{Four coils:}\quad & N_i = 2,\ L_i = 8,\ R_i = 12.26\,\mathrm{mm},\ d_i = 5.02\,\mathrm{mm}, \\
& N_a = 13,\ L_a = 12,\ R_a = 12.26\,\mathrm{mm},\ d_a = 7.42\,\mathrm{mm}
\end{aligned}$$

All the configurations exhibit nearly perfect homogeneity within the radii of the particle's motion and have a vanishing B_2 coefficient, making them suitable for our needs. The optimal four-coil configuration effectively reduces to a two-coil system because the two coils on each side are connected, though the coils differ in the number of layers. More precise, the outer coil has four layers more than the inner one.
In figure 4.4 the same plot is shown, but for wire with a diameter of 0.5 mm. The optimal configurations are:

$$\begin{aligned}
\textbf{Two coils:}\quad & N = 8,\ L = 7,\ R = 12.26\,\mathrm{mm},\ d = 7.15\,\mathrm{mm} \\
\textbf{Three coils:}\quad & N_i = 3,\ L_i = 1,\ R_i = 15.72\,\mathrm{mm},\ N_a = 8, \\
& L_a = 7,\ R_a = 12.26\,\mathrm{mm},\ d_a = 7.30\,\mathrm{mm} \\
\textbf{Four coils:}\quad & N_i = 5,\ L_i = 3,\ R_i = 12.26\,\mathrm{mm},\ d_i = 5.30\,\mathrm{mm}, \\
& N_a = 5, L_a = 7,\ R_a = 12.26\,\mathrm{mm},\ d_a = 8.00\,\mathrm{mm}
\end{aligned}$$

It is observed that even with twice the current, the coil configurations using the 0.5 mm wire produce a significantly weaker B_0-field. This is due to the fewer number of windings and layers that can be placed in the same volume. Given that and the fact that the thinner wire is much easier to handle, the 0.3 mm wire is found to be the better choice for the B_0-coil. Among the three configurations for the 0.3 mm wire, the four-coil setup performs best.

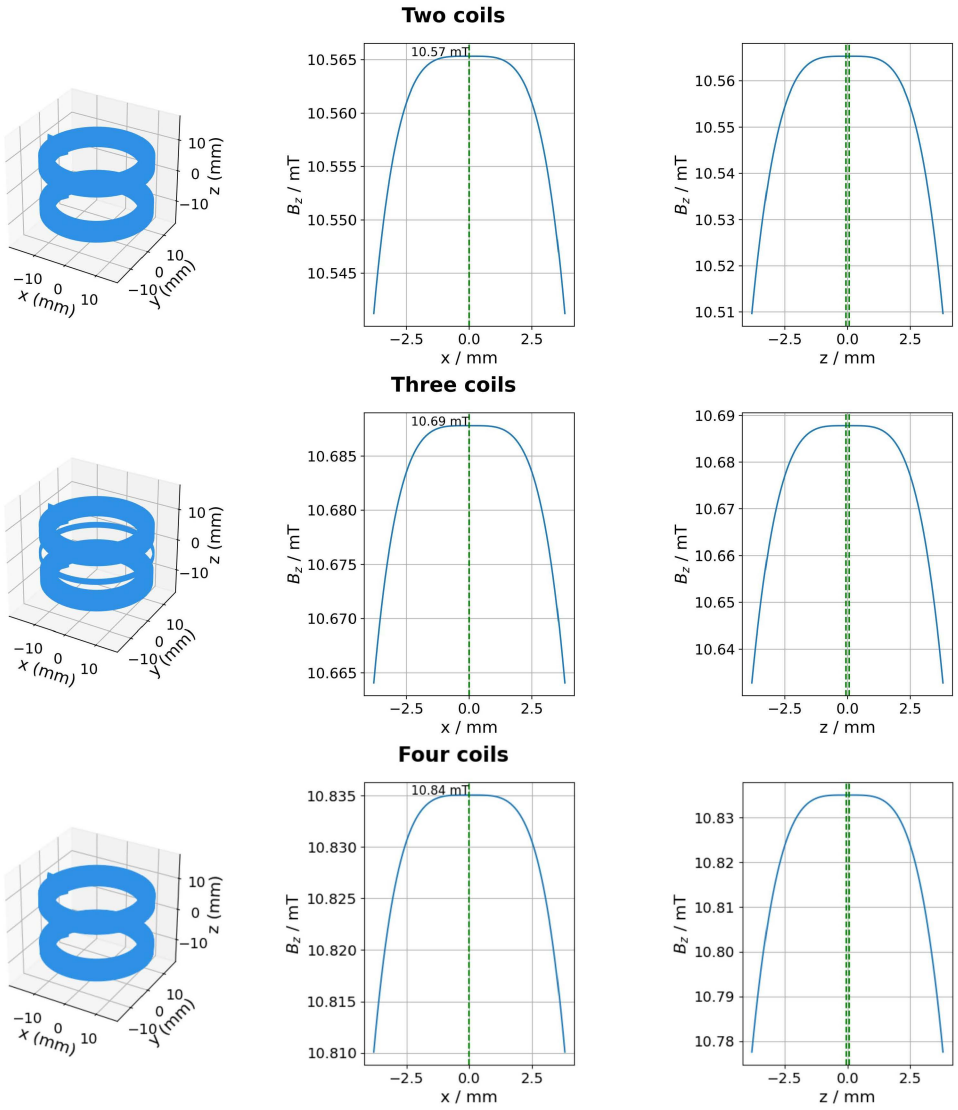

Figure 4.3: An overview of the different optimized geometries for two, three, and four coils. The B-field is illustrated along both the z- and x-axes. Additionally, the radius of the magnetron motion is plotted in green alongside the B-field in the x-direction and the axial amplitude alongside the z-direction. The four coils effectively merge together and therefore, look like a two coil system

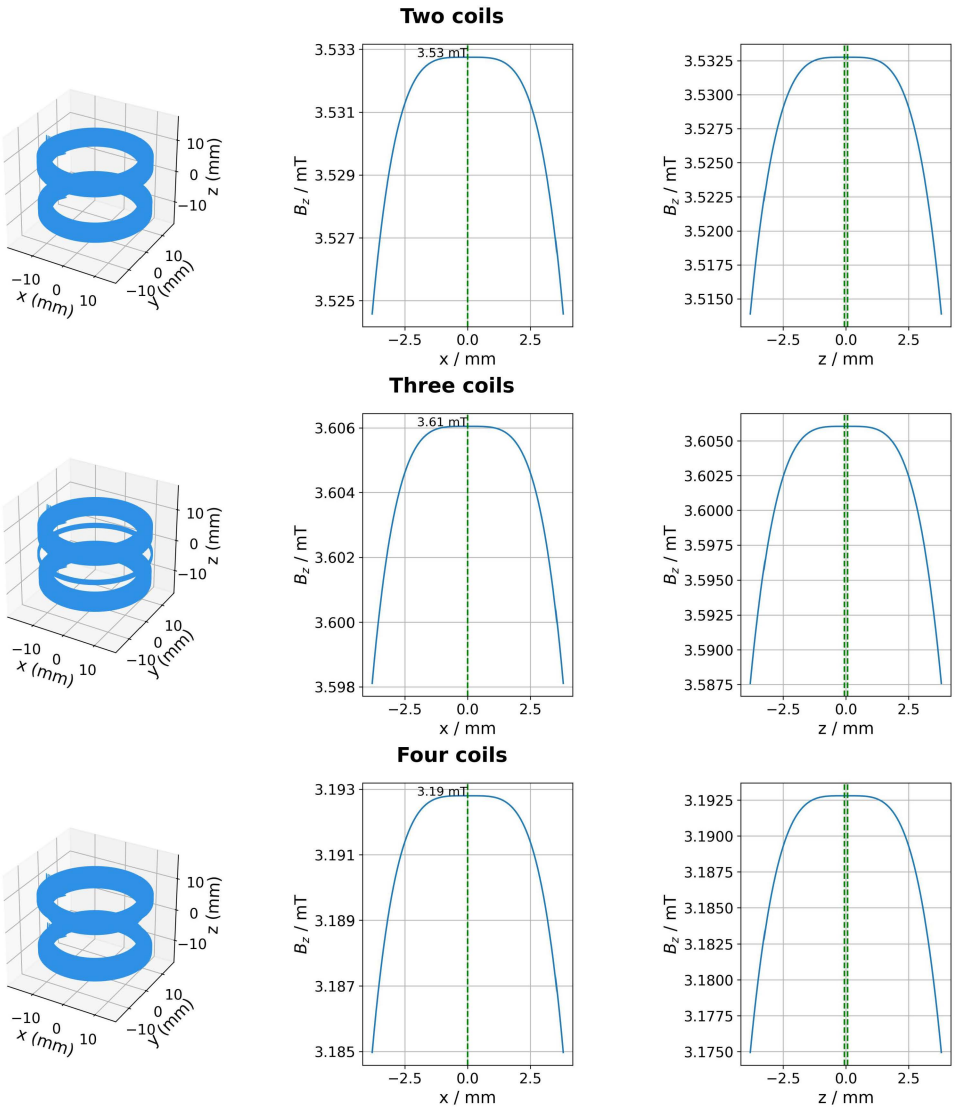

Figure 4.4: Optimization result for $d_{\text{wire}} = 0.5\,\text{mm}$. Again, the four coil simulation effectively connects to a geometry with two coils, but with a different number of layers.

However, given the small performance differences, opting for the simpler geometry is advantageous. This approach reduces manufacturing challenges and deviations from the ideal calculated results. Looking at the results of the three-coil system, it's clear that this configuration is not optimal. It performs only slightly better than the other two, but the additional coil introduces manufacturing challenges. Comparing the two-coil system and the four-coil system, it is also evident, that the ease of manufacturing the two-coil configuration is more advantageous than the small better performance of the four-coil system. Therefore, the two-coil system is the best choice.
When reviewing the results, it is important to note that all simulations are based on the approximation of planar loops, without accounting for the slight tilting of individual loops that occurs in actual winding processes. The deviations arising from this tilting are not addressed within the scope of this thesis, because their impact is assumed to be minuscule. Given the magnetic field of the tuning coil, the maximum frequency shift can now be calculated using equation (2.7), to be on the order of $\mathcal{O}(1\,\mathrm{GHz})$ for a current around 1 A.

Chapter 5

Development of a joint test setup

To test whether the joint is superconducting, a specialized test setup is developed. In this setup, different methods for joining the wire are tested.
The test setup consists of two coils nested within each other. One coil, the excitation coil, is connected to a power supply, while the other, the joint coil, includes the superconducting joint. This coil is a closed loop and has no connection to a power supply. When a voltage is applied to the excitation coil, a current flows through it, generating a magnetic field. As a consequence of electromagnetic induction and Lenz's law, the joint coil will create a counteracting field, causing a current to flow through it. If the joint coil is superconducting, this current should remain constant, resulting in a stable magnetic field generated by the joint coil. This field is measured with a magnetic field sensor.
The setup is subject to several requirements that must be considered during the design process. First, the entire experiment needs to be conducted in an ambient temperature of below 10 K, as the joints only exhibit superconductivity at low temperatures. Therefore, the setup is mounted on a closed cycle cryocooler, that can reach 4 K, and designed to be easily attachable to it. Additionally, the setup must facilitate quick and iterative changes to enable a fast testing process, since multiple joints are tested. Another critical requirement is the ability to send a high current through the test coil, potentially up to the critical current I_C, to fully evaluate the joint's performance. Finally, the setup must provide the ability to calibrate the sensor, because there is no data available for a temperature of 4 K. This calibration is performed with the excitation coil, and the results are shown in section 5.2.

5.1 Design of the test setup

To meet the requirements outlined above, the design depicted in figure 5.1 is selected. This setup comprises an adapter plate, an excitation coil, a joint coil, and an NVE AA005-02e magnet sensor [66]. The excitation coil is permanently mounted on the adapter plate, which

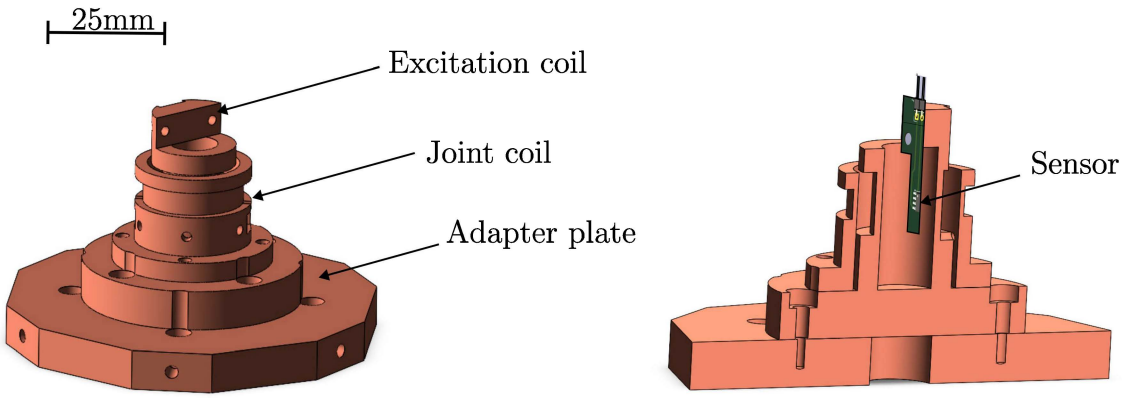

Figure 5.1: Setup for the coldhead: The setup for measurements in the coldhead is illustrated as follows: (left) the complete setup and (right) a sliced view of the setup featuring the NVE AA005-02e sensor. The pins of the sensor are connected to a voltage supply and a multimeter for reading out the measurements. The images show the different components that can be stacked on top of each other. The adapter plate can be screwed on the coldhead.

can be fixed on the coldhead. This coil is connected to a power supply and is responsible for inducing a current in the joint coil. To achieve this, the excitation coil has significantly more windings than the joint coil, enabling it to induce a high current in the joint coil from a relatively small input current. The magnet sensor is positioned in the center of the excitation coil. The joint coil can be assembled on top of this setup using four screws. To ensure accurate calibration of the sensor in a cryogenic environment, it is crucial that the magnetic field produced by the excitation coil is either homogeneous across the sensor's dimensions or that any variations in the magnetic field strength in the x- and z-directions are almost identical for both coils. Due to spatial constraints, simulating a coil with a perfectly homogeneous magnetic field is not feasible, leading to the choice of the second method. This means, that the field created by the two different coils should be nearly identical in shape. This approach is necessary because the sensor's calibration relies on the assumption that the measurement occurs at the sensor's center. If the actual measurement position deviates from this center, the sensor's output for a given magnetic field is overestimated, leading to an inaccurate calibration. To address this issue, the dependencies of the field produced by the excitation coil and the joint coil must be consistent. Additionally, the two coils must not be displaced relative to each other, so the center of both coils has to be at the same z-coordinate. This is ensured by the design and the mounting.
If the measurement electronics are positioned 1 mm off-center and the magnetic field at this position is 5 % weaker than at the center, the calibration overestimates the magnetic field by 5 %. When the joint coil is also measured 1 mm off-center, the calibration will similarly overestimate the magnetic field by 5 %, if the two fields have the same shape, compensating

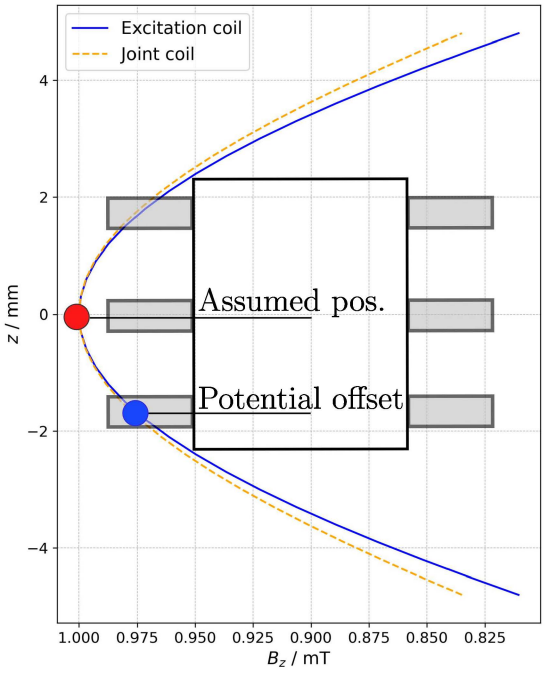

Figure 5.2: Calibration principle for the sensor. If the actual measurement electronics is placed somewhere away from the center, the same offset is present in the measurement of the joint coil and therefore cancels out. To ensure this, the two coils have to be mounted in a way that their centers are not shifted relative to each other. The field strengths shown in this plot are both normalized to the value at the center of the corresponding coil.

for the weaker field. Thus, the calibration correctly adjusts for the measurement position discrepancy, ensuring accurate field readings. The principle of this calibration process is illustrated in figure 5.2. To ensure this, the parameters of the excitation coil are fixed to 24 windings, 5 layers, and a radius of 7.5 mm. With these parameters, a configuration for the joint coil is determined to produce a field identical to the excitation coil. The choice is made to use the fewest windings possible for the joint coil to maximize the induced current in the joint loop. This optimization is performed for joint coils with wire diameters of 0.5 mm and 0.3 mm, as joints for both diameters are tested. The optimal parameters are as follows: for the thin wire (0.3 mm), the configuration is 20 windings with a radius of 12.5 mm; for the thick wire (0.5 mm), the configuration is 10 windings with a radius of again 12.5 mm. As one can see in figure 5.3 the deviations are less than 1 % within the size of the sensor. The final component that needs to be included in the setup is a heater to quench the joint coil. To quench it, a section of the coil must reach the critical temperature of NbTi, which is approximately 10 K. This requires a temperature increase by 6 K.
Given that the specific heat capacity of NbTi is approximately 0.6 mJ/gK at 4.2 K [67], and

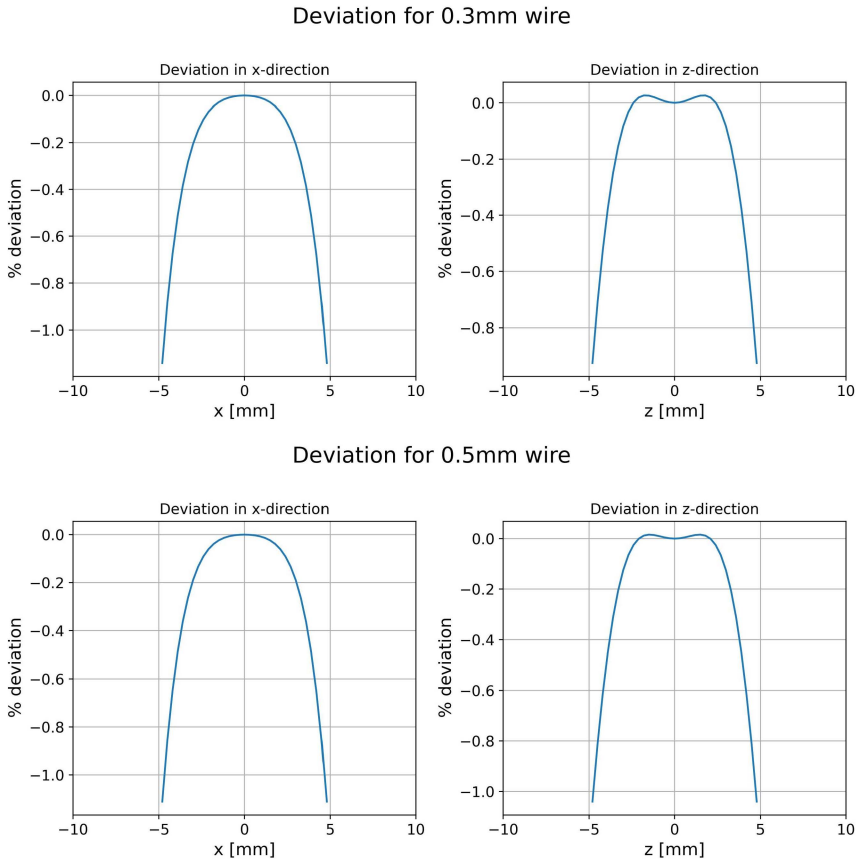

Figure 5.3: Deviations of the magnetic field created by the joint and the excitation coil in x- and z-direction. The sensor is 3.9 mm × 5.4 mm big, so the deviation is well below 1 % within the sensor's dimensions.

assuming that roughly 2 cm of the wire are heated, the required energy is calculated to be around 0.03 mJ. This amount of energy can easily be provided by a 10 Ω resistor. The energy dissipated by the resistor with resistance R in the time t is given by $E = R \cdot I^2 \cdot t$. For example, applying a current of $I = 0.01\,\text{A}$ for $t = 0.2\,\text{s}$ would, in theory, be sufficient to quench the coil. Considering all possible losses, a current of $I = 0.1\,\text{A}$, applied for half a second, should definitely be sufficient to quench the coil. A high quenching current isn't an issue, as everything will cool back down to 4.2 K after a few minutes of waiting.

5.2 Calibration of NVE AA005-02e sensor at 4 K

As already mentioned, the calibration is performed using the excitation coil. To do this, the excitation coil is mounted on the coldhead and cooled down to 4 K. The magnetic field generated by the coil for different currents can be calculated as a superposition of the contributions from all windings, according to equation (2.25). By comparing these calculated

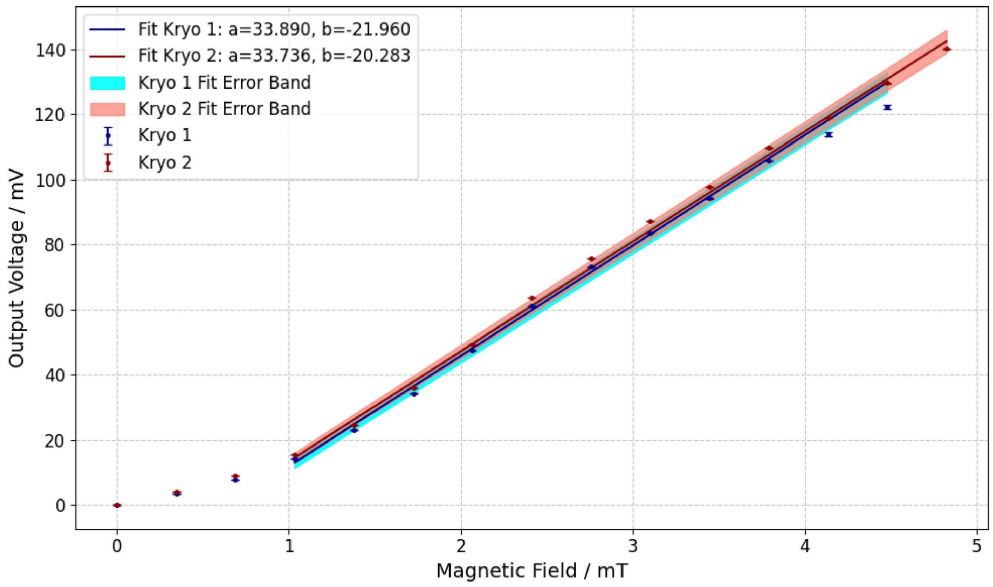

Figure 5.4: Calibration measurement for the NVE AA005-02e sensor. Two measurement series were performed. A linear function is fitted to the values between 1 mT and 7 mT. One can see the deviation from a linear behavior for small magnetic fields. That also explains why one doesn't get a straight origin line as a fit. The colored areas are the error bands of the fits.

values with the sensor's measured outputs, the sensor can be calibrated.
According to the sensor's data sheet, its linear range is between 1 mT and 7 mT. Therefore, the values within this range are fitted using a linear function $f(x) = ax + b$. The results are shown in figure 5.4. The measurement is performed twice, thereby improving statistical significance and to check for reproducibility. The two resulting fits are averaged, leading to the final calibration:

$$B[\mathrm{mT}](V_{\mathrm{out}}) = \frac{V_{\mathrm{out}} + b}{a} = \frac{V_{\mathrm{out}} + 21.12\,\mathrm{mV}}{33.8\,\frac{\mathrm{mV}}{\mathrm{mT}}} \tag{5.1}$$

With equation (5.1), the magnetic field for a certain sensor-output can be calculated. The offset of 21.12 mV can be explained with the fact that the linear range starts above 1 mT, so for small outputs the linear fit doesn't give the right B-field. The corresponding error ΔB is given by the error of the measured voltage and the error of the fit,

$$\begin{aligned}\Delta B &= \sqrt{\left(\frac{\Delta V_{\mathrm{out}}}{\bar{a}}\right)^2 + \left(\frac{\Delta \bar{b}}{\bar{a}}\right)^2 + \left(\frac{V_{\mathrm{out}} + \bar{b}}{\bar{a}^2}\Delta\bar{a}\right)^2} \\ &= \sqrt{\left(\frac{\Delta V_{\mathrm{out}}}{33.8\,\frac{\mathrm{mV}}{\mathrm{mT}}}\right)^2 + \left(\frac{0.74\,\mathrm{mV}}{33.8\,\frac{\mathrm{mV}}{\mathrm{mT}}}\right)^2 + \left(\frac{V_{\mathrm{out}} + 21.12\,\mathrm{mV}}{\left(33.8\,\frac{\mathrm{mV}}{\mathrm{mT}}\right)^2}0.034\,\frac{\mathrm{mV}}{\mathrm{mT}}\right)^2},\end{aligned} \tag{5.2}$$

where the bars indicate an average of both fits. The desired current to create a measured field

strength with the configuration of the joint coil can then be calculated using a superposition of equation (2.25). To also find a corresponding current for the field strengths below the linear threshold of 1 mT, the outputs in this region are fitted using a liner interpolation between the data points in this regime.

5.3 Production of superconducting joints

The following section discusses the production of the superconducting joints and the challenges encountered during this process. An overview of the production steps is provided in section 2.2.2, and here, each step is examined in greater detail.
A total of four different joints are fabricated: two using the thin wire (0.3 mm) and two using the thick wire (0.5 mm). All joints are made using a Lampert PUK-U5.
For each wire diameter, one joint is created by directly welding the wire ends together, and another by welding the wire onto a small NbTi cylinder. The cylinder measures 3 mm in diameter and 8 mm in length, featuring a small slit where the wires are positioned. A picture of a direct joint and one produced inside a cylinder is shown in figure 5.5. The fabrication process is as follows:
1. Removing the insulation: The insulation is mechanically removed using a stripper, leaving the bare surface of the copper matrix.
2. Etching the copper matrix: In the next step, the copper matrix is etched away using a 80 % nitric acid solution. This process takes approximately five minutes. To ensure successful etching, the wire should be gently moved within the acid. Additionally, it should be removed periodically from the acid and wiped down with a cloth in order to mechanically remove partially etched chunks, enabling etching of the layer underneath.
3. Cleaning the bare filaments: After etching, the exposed NbTi strands are thoroughly cleaned with ethanol and water. This ensures that no residual acid remains on the wire, providing a clean surface for welding.
4. Welding the wire: Finally, the welding process is carried out. For the joints without the NbTi cylinder, the two NbTi strands are twisted together, and several spot welds are placed along the helix. This approach ensures that at least one of the welds establishes a strong connection. During the weld, one of the wires is connected to the positive pole of the welding machine. The welding parameters are set to 22 % of the maximum power for 2.0 ms for the thin wire, and 24 % for 2.5 ms for the thick wire. These values are selected because they reliably produce a good weld without burning away the wire. However, the exact parameters may need to be fine-tuned. There is no perfect setting, as the weld quality depends on various factors like the positioning of the welding electrode, the bulk clamp placement, and the argon inert gas pressure. Therefore, one has to play a little with the settings to achieve optimal weld quality.

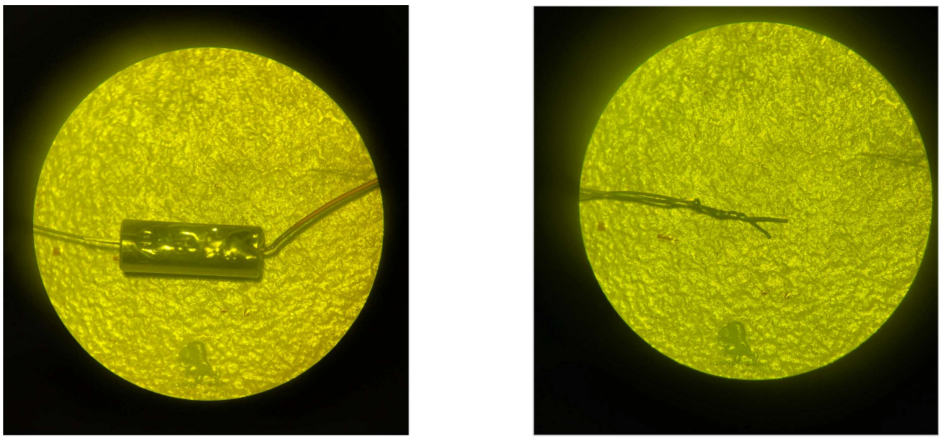

Figure 5.5: Pictures of the superconducting joints taken under a microscope. (Left) The joint is produced inside a small cylinder. For this, the wires are placed inside a small slit in the cylinder. (Right) The joint is produced by welding the two wires directly together. One can see the twisted wires and the several spot welds.

For the joints involving the NbTi cylinder, each wire is welded separately within the slit of the cylinder. The welding parameters for these joints are 24 % for 2.5 ms for the thin wire and 28 % for 3.0 ms for the thick wire. Here, the plus pole is connected to the cylinder. The advantage of using the cylinder is the easier handling and the welds can be performed smoother. On the downside of this method is that the cylinder requires a lot of space.

5.4 Measurements and results

5.4.1 Measurement procedure

To evaluate the performance of the different joints, the setup shown in figure 5.1 is mounted onto the coldhead and cooled down to 4 K. The sensor's pins are connected to a voltage supply and a multimeter for data readout, utilizing the connections on the coldhead. Additionally, the heater and the excitation coil are connected to a power supply through the coldhead pins. The measurement process follows this scheme:

1. Send a current through the excitation coil. This creates a magnetic field and induces a current in the joint coil. Since the joint coil is superconducting, the induced current will persist indefinitely, maintaining the counteracting magnetic field as long as the coil remains in a superconducting state. However, the field of the excitation coil is stronger than the counteracting field, so a magnetic field can be measured with the sensor.

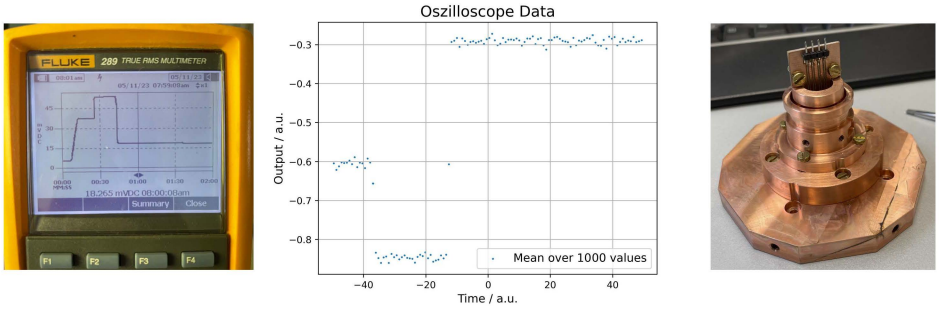

Figure 5.6: Measured signals and the test setup. (Left) Real data captured with an oscilloscope and a multimeter. The measurements show how the voltage output changes during the different stages of the experiment. For the oscilloscope, the first constant tail when all coils are turned off isn't plotted. (Right) Picture of the real setup used for the joint test.

2. Quench the joint coil. For about half a second a current of 100 mA is sent through the resistor, heating it up above T_C of NbTi. As a consequence, the current in the joint coil decays and the total magnetic field increases, because the field of the joint coil is counteracting the field of the excitation coil. After the quench, one has to wait for roughly ten seconds until the joint coil is thermalized again to 4 K.

3. Turn off the excitation coil. This will again induce a current in the joint coil due to the changing magnetic field. The advantage of this step is that now only the current in the joint coil remains, allowing the magnetic field it produces to be measured in isolation without interference from the excitation coil. In total, the magnetic field will decrease, because the field created by the excitation field is now absent.

The different steps of the measurement process are illustrated in figure 5.7. This figure clearly shows how the magnetic field initially increases as current is applied to the excitation coil. After quenching the joint coil, the magnetic field rises even further because the counteracting field produced by the joint coil is no longer present. Once the excitation coil current is turned off, the magnetic field decreases, leaving only the field generated by the joint coil. This final step allows for an isolated measurement of the joint coil's magnetic field, confirming its superconducting properties. The measurement procedure was repeated for excitation values from $I = 50\,\text{mA}$ up to 500 mA in steps of 50 mA. For all values the ouput voltage of the NVE AA005-02e was notated and an estimate for the error is made by the fluctuations of the output.

5.4.2 Results

General observations: The estimation of the error in the measurements is quite challenging due to fluctuations and occasional drift in the sensor output. The exact cause of

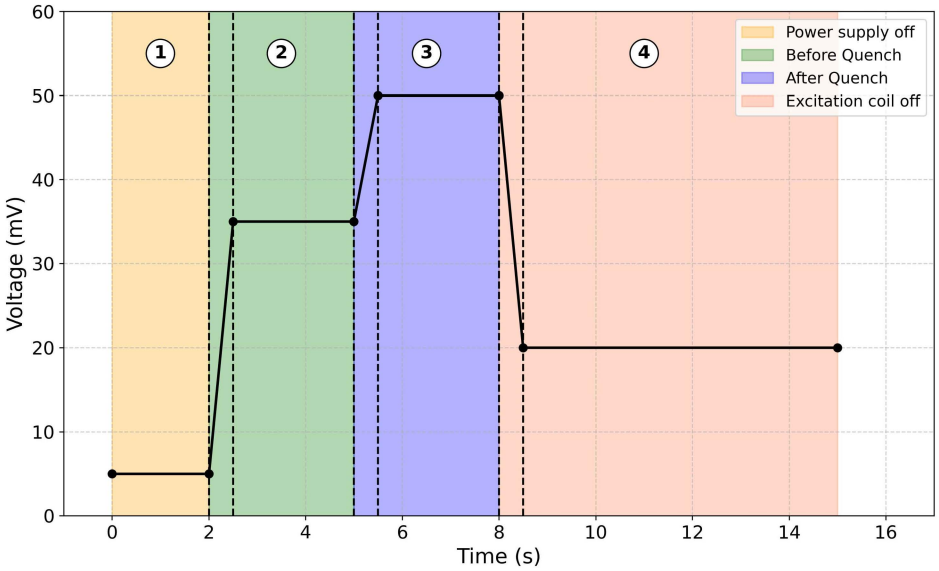

Figure 5.7: A schematic representation of the voltage output corresponding to the various steps in the measurement process. (1) Both coils turned off. (2) Excitation coil turned on, inducing a current in the joint coil. (3) The magnetic field rises after the joint coil is quenched. (4) The excitation coil is turned off, again inducing a current in the joint coil. The final constant tail in the output indicates the persistent current in the joint coil, confirming its superconducting state. This persistence demonstrates that even after the excitation coil is turned off, the current induced in the joint coil remains, producing a stable magnetic field.

this drift remains undetermined, though several factors could be responsible. These include heating within the setup due to Ohmic heating of the excitation coil, magnetization of nearby components, or interactions between the coils. However, since the drift is not consistently observed across all measurements, it is difficult to pinpoint the exact cause.

Additionally, the sensor's offset, so the output value at zero background field, exhibits significant variation during the measurement, varying from $-7\,\mathrm{mV}$ to $7\,\mathrm{mV}$. This is mainly caused by the hysteresis effect of the sensor. According to the data sheet, the maximum hysteresis is $4\,\%$ resulting in a deviation of roughly $3.5\,\mathrm{mV}$ for outputs up to $90\,\mathrm{mV}$. Yet, it is important to notice, that the values from the data sheet are taken for a temperature range down to $-50\,^{\circ}\mathrm{C}$, so maybe in a cryogenic environment, the hysteresis can be larger.

In the following, a direct joint refers to a connection where the two wires are joined without using a NbTi cylinder, whereas a cylinder joint involves the use of a NbTi cylinder.

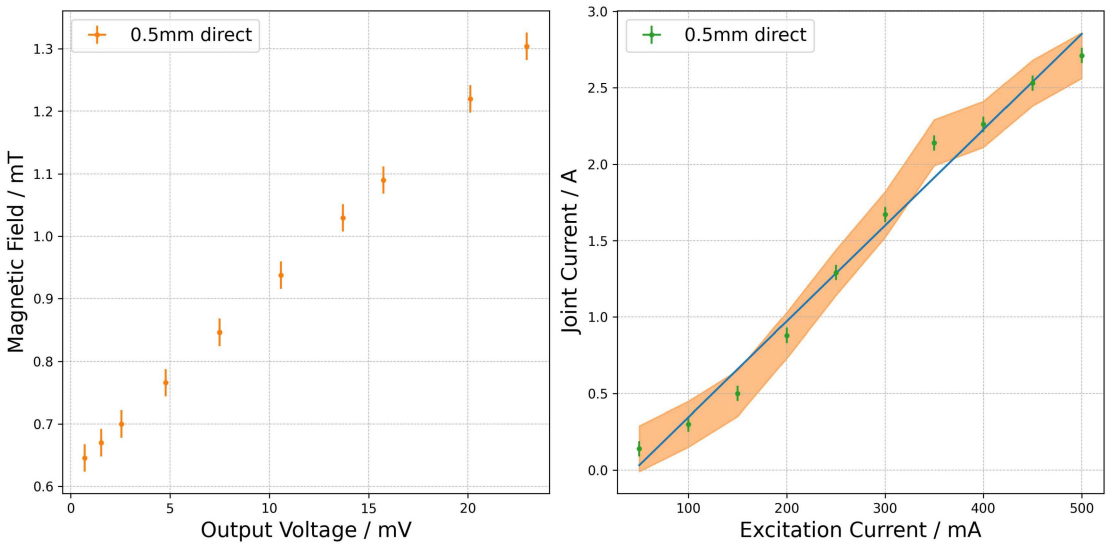

Figure 5.8: Result of the measurement for the 0.5 mm direct joint. (Left) The measured output voltage and the corresponding magnetic field is plotted. The magnetic field is calculated with the fit in equation (5.1). (Right) The calculated current to create the magnetic fields is measured against the current in the excitation coil. Also, a linear fit to the data is given, as one would expect a linear dependency between the joint and the excitation current. The orange band shows the $3\,\sigma$-range to outline significant deviations from the linear fit.

0.5 mm direct: In figure 5.8, the measurements for the joint are presented. The results show that a current of over 2.5 A is achieved. Up to this current, the joint remains superconducting. Higher excitation, and therefore higher joint currents, can not be tested with the current setup due to limitations of the power supply. Throughout all joint currents, the joint coil remains superconducting, and over a span of several minutes, no decay is observed. It is noteworthy that the linear fit to the joint currents generally lies within the $3\,\sigma$-region, though some measurements deviate from it. This suggests that either fluctuations in the output voltages or the assumed errors are underestimated. Besides, it could be that the sensor has some kind of non-linearity at an ambient temperature of 4.2 K
Nevertheless, the direct joint demonstrates good performance, achieving a high critical current.

0.5 mm cylinder: For the joint made with the thick wire and the NbTi cylinder, the performance is quite similar to that of the joint without the cylinder. As shown in figure 5.9, a current exceeding 2.5 A is again achieved without losing superconductivity. Additionally, the linear fit appears slightly improved, with all values falling well within the $3\,\sigma$-range.

0.3 mm direct: In the figure 5.10, the results for the direct joint made with the thin wire are presented. The direct joint remains superconducting up to a current of approximately

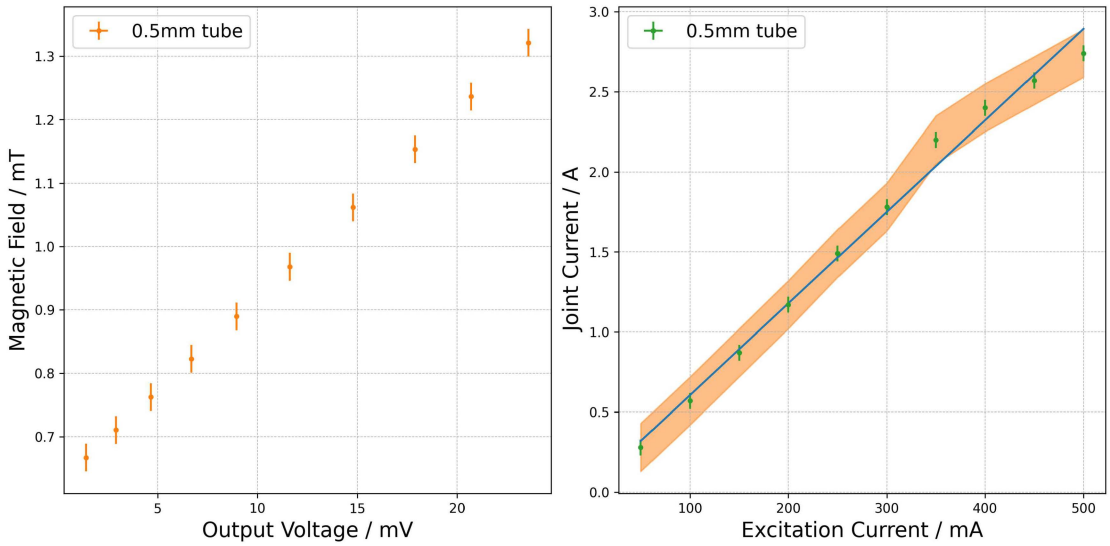

Figure 5.9: Results for the measurement with a 0.5 mm wire and a NbTi cylinder to perform the joint.

1.4 A. Again, higher currents were not tested, due to the limitations of the power supply. The linear fit, however, shows poor performance, indicating the presence of some non-linearity in this measurement.
Notably, the joint current for an excitation current of 50 mA seems unreasonable, as it is only slightly above 0 A. This data point is likely incorrect, possibly due to an error in the measurement procedure. It's possible that the offset is incorrectly determined, leading to a smaller output voltage and, consequently, an inaccurately low current. Additionally, the two values for excitation currents of $I = 150\,\text{mA}$ and $I = 350\,\text{mA}$ differ significantly from the linear fit. Likely, this is caused by the strong fluctuations of the sensor output.

0.3 mm cylinder: The performance of the cylinder joint for the thin wire, shown in figure 5.11, is quite similar to that of the direct joint, also remaining superconducting up to approximately 1.4 A. In this case, the linear fit appears to be quite accurate, indicating that no significant errors occurred during the measurement process.
Comparing the thin and thick joints, it is observed that for each excitation current, the current in the joint loop is roughly twice as high in the thick wire. This is expected, as the thin joint coil consists of 20 windings, while the thick joint coil has only 10 windings.

In addition to these measurements, one measurement with the 0.5 mm direct joint is conducted over a 3 h period. No significant decay is observed within this time frame, further indicating that the joint is superconducting. This can be seen even in a shorter period, as a non-superconducting joint would heat up due to resistive losses, which would increase its resistivity and cause further heating. Consequently, the current would decay rapidly.

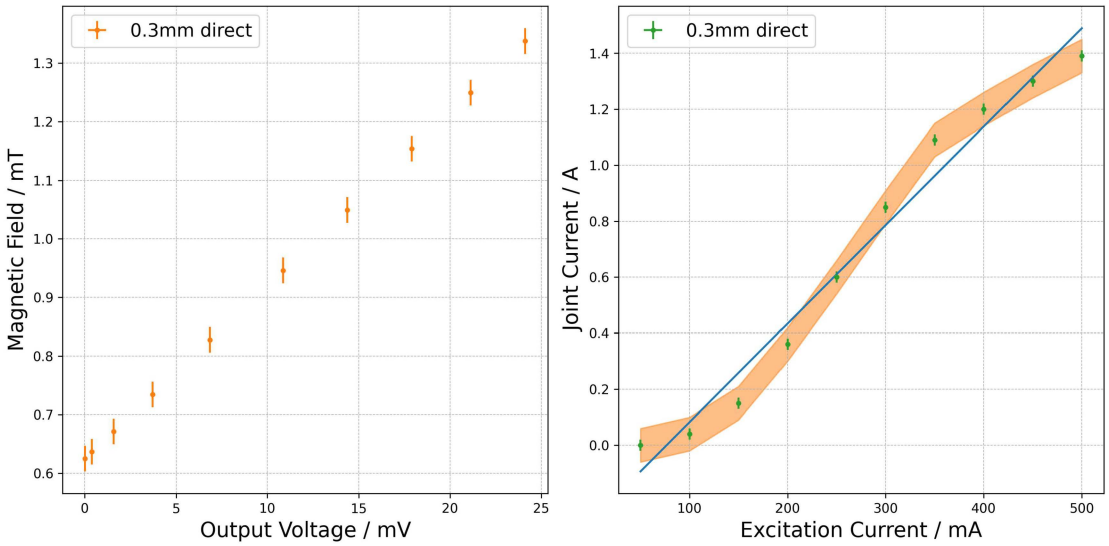

Figure 5.10: Results for the measurement with the 0.3 mm direct joint.

In summary, all joints perform well and remain superconducting at the maximum injected current. None of the joints reach their critical current, indicating that all techniques used are effective and suitable.

The thin wire allows for significantly more windings, resulting in a higher achievable magnetic field, even with only half the current of the thick wire. This means that using the thin wire, it is possible to achieve geometries that outperform the best configurations of the thick wire, despite using much less current.

In addition to that, considering the manufacturing process, the thin wire emerges as the better choice as it is much easier to wind coils with the thin wire, making it the preferred option.

Between the direct and cylinder techniques, the differences are very little. The cylinder technique is a bit easier to manufacture and provides a higher mechanical stability. However, this stability can also be reached with the direct joint when covering the joint with epoxy. The disadvantage of the cylinder joint is the required space, as the cylinder has a dimension of approximately 8 mm in height and 3 mm in diameter. Since there is no clear-favored technique, the measurement in the following chapter is performed with the direct technique.

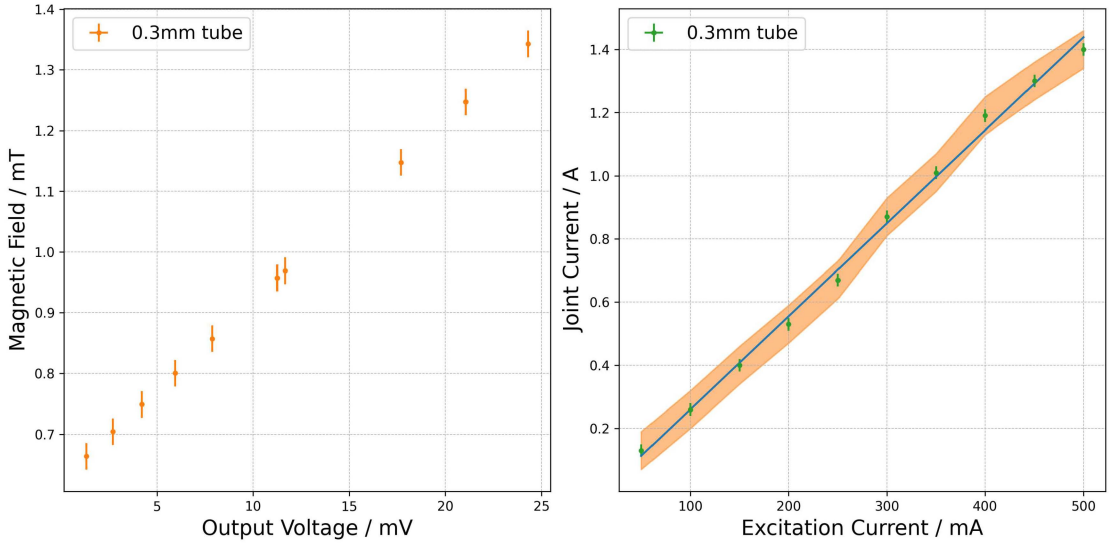

Figure 5.11: Results for the measurement with the 0.3 mm cylinder joint.

Chapter 6

Joint tests in the ELCOTRAP experiment

As discussed in section 2.1.5, the joint must be tested in a strong background field because the magnetic field in ELCOTRAP could potentially reach the critical magnetic field (B_C) of the joints, causing them to lose their superconductivity. Consequently, the 0.3 mm wire direct joint, which showed good performance in the experiment described in chapter 5, is tested in the 7 T magnet of ELCOTRAP.

6.1 Basic idea and experimental setup

To test the joint, a NbTi coil, including the joint, is wrapped around the trap chamber in which the Penning trap is located. A second coil, wound bifilarly with this coil, is connected to a power supply and used as an excitation coil. Once a current is sent through the excitation coil, it induces a current in the joint coil. The excitation coil is made with a 0.5 mm wire, while the joint coil is made of the thinner 0.3 mm wire. Each coil consists of 20 windings, with a coil radius of 50.5 mm. Both coils have only one layer. Using equation (2.25) and applying the superposition principle while neglecting the small helix-like structure, the joint coil should generate a magnetic field of around 0.025 mT for an excitation current of $I_{exc} = 0.1$ A, corresponding to a shift of the free cyclotron frequency of roughly 1 kHz for a fully ionized carbon atom. This frequency shift can be measured using the FT-ICR method described in section 2.1.5.
Additionally, a heater is required to quench the coil. This heater is constructed using a manganin wire that is wrapped, together with a small piece of the wire of the joint coil, around a circuit board. When a current flows through the manganin wire, it heats up the joint coil wire due to Ohmic dissipation. The heater consists of six windings with each having a length of approximately 24 mm, leading to a resistance of $R = l \cdot \rho = 1.94\,\Omega$, where l is the length of the wire and ρ is the specific resistance of manganin, which is 13.5 Ω/m at 4.2 K [68]. For a current of 0.1 A, this results in a heating power of approximately 19.4 mW,

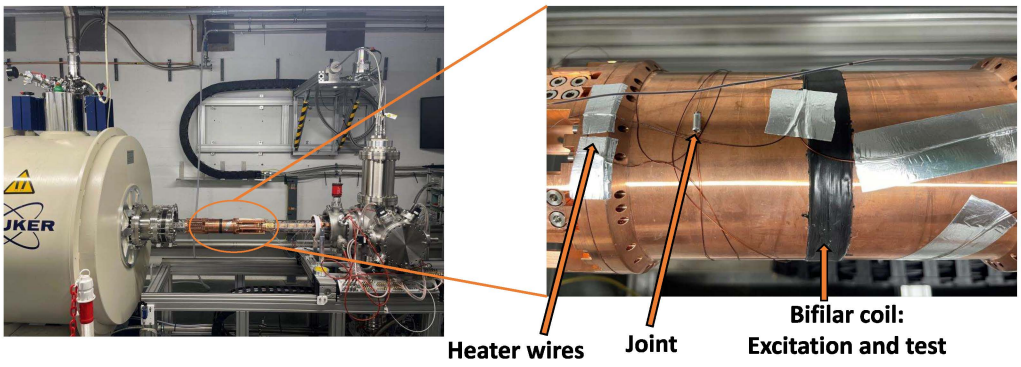

Figure 6.1: Setup for the joint test in the ELCOTRAP experiment. The heater is placed next to the trap chamber and screwed on the 4 K stage. The two coils are fixed on the trap chamber with LOCTITE STYCAST 2850FT epoxy. In this attempt the joint is produced with the cylinder, which was found to be mechanically broken after the first cooldown. The results reported below are performed with a different joint.

which is easily sufficient to quench the coil. To better isolate the heater from the rest of the coil, the copper matrix on the wires leading to the heater is etched away, reducing the thermal conductivity of the wire. The whole setup is shown in figure 6.1.

6.2 Measurement process

Loading Ions: Before starting the actual measurement, an ion must be loaded into the trap. In ELCOTRAP, ions can be produced directly inside the trap. This is achieved by applying a high voltage to a cathode, which creates a strong electrostatic field that induces field electron emission. These emitted electrons hit a carbon target and have enough energy, in this case $\sim 1\,\mathrm{keV}$, to fully ionize the carbon atom, thus a $^{12}C^{6+}$ ion can be loaded. During this process, other ions or multiple carbon ions may also become trapped unintentionally. To isolate the desired ions, the unwanted ones must be removed using the burst technique, as described in section 2.1.3.

Measurement procedure: The measurement procedure follows the same steps outlined in chapter 5. First, a current is passed through the excitation coil, which induces a current in the joint coil. The joint coil is then quenched, and subsequently, the excitation coil is switched off, once again inducing a current in the joint coil. At this point, the joint coil should generate a stable magnetic field.
To measure the frequency shift, different frequencies must be measured. For this, first the axial frequency is measured using the FT-ICR method described in section 2.1.5. Afterwards,

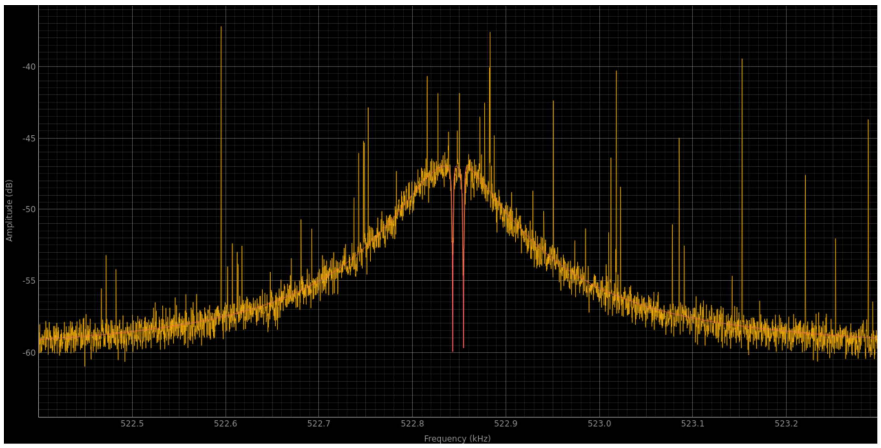

Figure 6.2: Double dip spectrum in ELCOTRAP. The red line indicates the fit for the double dip. The peaks on the spectrum are noise peaks.

the axial motion is coupled to the modified cyclotron motion using an RF-field. As outlined in section 3.2, this leads to an energy transfer between the two modes and to a splitting of the detected axial signal. Instead of a single axial dip, now a double dip is present [16]. The frequencies of the double dip are related to the modified cyclotron motion by

$$\omega_+ = \omega_{RF} - \omega_z + \omega_l + \omega_r, \tag{6.1}$$

where ω_r and ω_l are the frequencies of the left and right dip, respectively. An example of such a double dip is shown in figure 6.2. For performing a quantitative evaluation of the frequency shift due to the magnetic field, all eigenfrequencies must be measured and afterwards, the free cyclotron motion can be calculated and used to determine the additional B-field. However, for a first estimate a measurement of the modified cyclotron motion with equation (6.1) is sufficient.

6.3 Measurement results

Once the excitation coil is turned on, one would expect to see no phase shift. If the joint coil is superconducting, it would create a counteracting field, and the field of the excitation coil and the joint coil would exactly cancel out, resulting in no frequency shift. Due to small deviations, a small frequency shift may be present. In figure 6.3 the measured frequncies are shown. One sees a clear shift of them, once the excitation coil is turned on. This indicates that the joint coil is not superconducting. Also, quenching the joint coil doesn't make any difference, what again shows, that the joint or some other part of the coil is not superconducting. As a result, the joint coil is not able to produce a stable magnetic field. The reason why the joint is not superconducting cannot be said with certainty. One possible

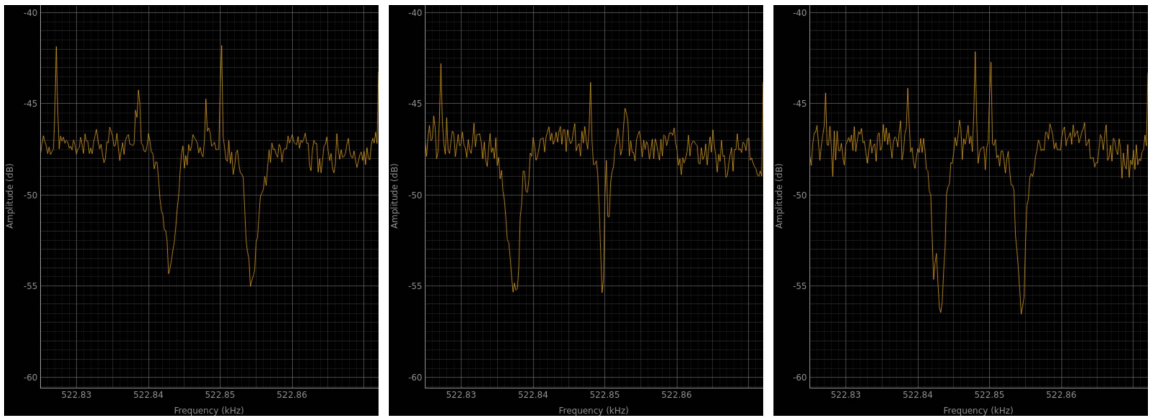

Figure 6.3: Recorded double dips in the ELCOTRAP experiment. On the left side, the excitation coil is off. In the middle, the excitation coil carrys a current of 1 mA leading to a frequency shift of the double dip. If the joint coil would be superconducting, no shift should occur. On the right side, the excitation coil is turned off again after the joint coil was quenched, and the same dip spectrum is present like on the left side, indicating that no current is flowing through the joint coil.

explanation is that a part of the coil is not properly cooled to below 10 K, and hence, not superconducting. In the setup, the temperature at the cooldhead is measured to be 4.3 K, on the coldhead side the temperature is 5.9 K and on the other side it is 7.5 K. However, it is possible that some parts of the system are hotter. This can especially be the case for the heater, because in the design it is aimed to decouple the heater thermally from the rest of the setup. This might lead to an ineffective cooling, preventing the heater from reaching a temperature below 10 K. This effect can even be enhanced by radiation of the heat shield heating up the heater. It could also be the case that after quenching and turning off the heater, the heater is not adequately cooled. However, this effect can usually be mitigated by waiting a few minutes between quenching and switching off the excitation coil. But even after waiting a few minutes between quenching and turning off the excitation coil, the joint coil is still not superconducting. To test whether the heater is cooled properly, another measurement will be performed with a temperature sensor placed at the heater position to investigate, if the heater is indeed not cold enough. However, this measurement can only be carried out after the submission of this thesis.

Another possibility is that the joint losses its superconductivity in the strong background field. This can be caused by impurities, like remaining copper or the oxidation of niobium or titanium that can occur during the welding process. Also, the heating to several thousand degrees might change the structure of NbTi, decreasing B_C. To check this hypothesis, it would be necessary to test the same joint in zero, or at least in a weaker, background field. In this way, one could investigate, if the joint is superconducting at all. Since all the joints in chapter 5 are superconducting it is quite unlikely, that the joint isn't superconducting at

all, but there is no literature available, about how the critical magnetic field changes during the welding process. Another possible reason is, that the joint breaks mechanically. This was the case in a prior measurement with a 0.3 mm cylinder joint. To avoid this, the joint was mechanically stabilized with epoxy.
However, yet it can not be said, what the actual problem is, and further investigations have to be made.

Chapter 7

Implementation of the tuning coil in ELCOTRAP

In this chapter, the design of the B_0-coil for later integration into ELCOTRAP is presented. Because the actual trap design of ELCOTRAP isn't finished yet, it is possible that minor changes to the dimensions will be made for the final implementation. However, it shows which requirements a design must fulfill.

7.1 Design of the coil

Like the assemblies in the previous chapters, the basic components of the assembly are the coils itself, a heater, and some mechanism to induce a current in the coil. The complete setup is shown in figure 7.1. It is the two-coil configuration for the thin 0.3 mm wire simulated in chapter 4.

Due to space constraints, using an excitation coil to induce the current is impractical. Instead, the coil is directly connected to a power supply. To initiate the current flow in the coil, a small section between the two connections to the power supply is heated above its critical temperature, causing it to lose its superconductivity. This forces the current to flow through the superconducting coils rather than just along the short connection between the supply wires. Once the heated section cools back down and returns to a superconducting state, the power supply can be switched off. Thanks to the coil's self-inductance, it will generate and maintain a constant current within itself. A sketch of this is illustrated in figure 7.2. The left part with the two coils is superconducting, while the part on the right side is heated above T_C and therefore serves as a superconducting switch.

The heater consists of a manganin wire that is wrapped around a circuit board and connected to a power supply. When a current flows through the manganin wire, it heats up due to Ohmic dissipation. Additionally, a small section of the wire from the coil is wrapped

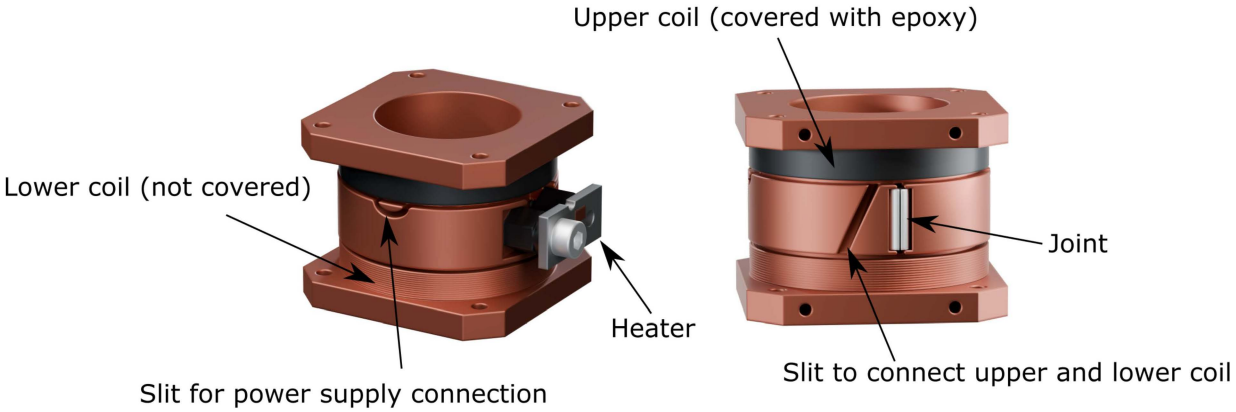

Figure 7.1: Assembly of the B_0 coil for the ELCOTRAP experiment. The left picture shows the front view with the heater and the slit on the left, where the power supply wire can be soldered. The right picture shows the cylinder for the joint and the slit through which the wire can be guided to come from the bottom to the top coil. For illustration, the upper coil is shown covered with epoxy, while the lower one isn't, so one can see the single windings.

between the windings of the manganin wire and heats up as well when the power supply is turned on, causing the coil to quench. To thermally isolated the heater from the rest of the assembly, it is placed away from the copper mount using small plastic spacers and the copper matrix is etched away.
The joint, either produced with a cylinder or by direct welding two ends together, can be placed in a milling hole and thermally coupled to the mount using epoxy. Also, the single windings are covered with epoxy to fix them and enhance their thermal coupling to the rest of the assembly.

When winding the coil, special care must be taken to minimize deviations from the calculated configuration outlined in section 4.2, as even minor imperfections can lead to unwanted field distortions. The winding process begins from the center of the assembly, starting with the lower coil. This coil is wound with 14 windings and 12 layers. The center of the coil is placed roughly 7 mm away from the middle of the coil mount. The wire is then passed through a slit in the center of the assembly to begin winding the upper coil.
In the upper coil, the wire is passed through slits on both sides and wrapped around the heater. At these slits, the insulation is removed to allow for soldering the power supply connections. In the section where the coil is wrapped around the heater, the copper matrix is etched away to reduce thermal conductivity, ensuring that the rest of the coil remains in a superconducting state. Once the upper coil is wrapped, the end of the wire can be passed in the small cutout where the joining can be performed.

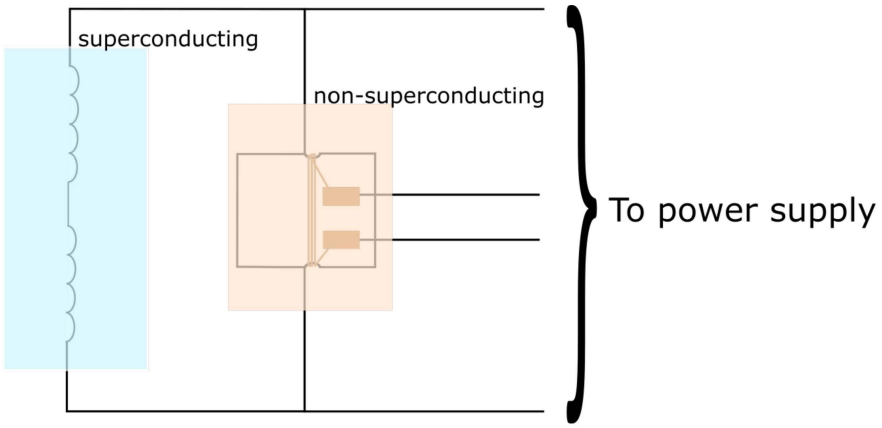

Figure 7.2: Schematic of the coil assembly. The coils are connected to a power supply, while the part between the two supply wires is heated. The blue area is superconducting, while the orange can be made normal conducting by heating the wire and hence, can serve as a superconducting switch. Once the heater-supply is turned off and the wire section between the supply wires is cooled down, the power supply can be turned off and a persistent current flows through the coils.

7.2 Installation in ELCOTRAP

The final installation of the tuning coil in ELCOTRAP is shown in figure 7.3. It is placed around the trap electrodes and secured to the piezo mount with four screws. This design ensures that the generated magnetic field is as homogeneous as possible, and everything is properly adjusted and fixed in the actual setup. Through the bottom of the coil, the piezo shown in figure 3.3 can be connected and used to adjust the trap dimensions.

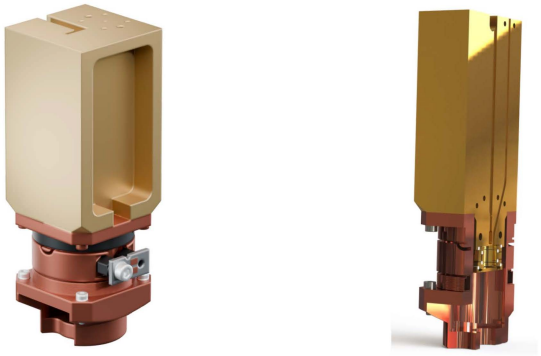

Figure 7.3: The whole setup in ELCOTRAP. (Left) Rendering of the setup. (Right) Sliced CAD-model of the setup. In the center is the actual trap with five electrodes. The top electrode is also used to inject the RF-field. Around these the tuning coil is mounted. Below the coil, a piezo motor is placed that can adjust the trap dimensions.

Once the final design of the trap is completed and the B_0 assembly is manufactured, it can be implemented in the actual experiment. If everything functions as expected, the B_0-coil can be used to shift the frequencies of trapped electrons, thereby matching them to the cavity modes of the trap. This will ensure proper cooling of the modified cyclotron motion in the ET and allow for the coupling of the axial and cyclotron motions. In this way, the axial motion will also be cooled and can be used to cool the ion in the IT.

Chapter 8

Summary and outlook

The goal of this thesis was to develop two types of superconducting coil assemblies for the Penning-trap experiment ELCOTRAP. One assembly was designed to be used for temperature measurements within the trap by generating a quadratic field gradient (B_2) inside the trap, while the purpose of the other was to create a homogeneous magnetic field to shift the frequencies of stored electrons in the trap. The temperature measurement was intended to verify the success of electron cooling, while the frequency shifts were necessary to match the eigenfrequencies of the stored particles to the cavity modes defined by the electromagnetic cavity formed by the trap electrodes.

To achieve this, suitable geometries were first calculated using a newly developed optimization scheme. This scheme employed a superposition of single loops to compute the total magnetic field of a coil configuration and optimize it within given boundary conditions, such as space constraints and the requirement for vanishing higher-order magnetic field dependencies. The optimization scheme was applied to two different wire diameters, namely 0.3 mm and 0.5 mm, and two assemblies with varying numbers of coils. It was found that a four-coil geometry provided the best configuration for achieving a high degree of magnetic field homogeneity within the space constraints of the experiment. However, when considering the manufacturing process, the two-coil configuration is the better choice, as fewer coils are easier to produce. The highest magnetic bottle effect was obtained by a three-coil geometry. The exact parameters are listed in chapter 4. Additionally, it became evident that the thinner wire coil could generate more than twice the field strength of the thicker wire with the same current, due to the ability to place significantly more windings in the same volume.

The simulation also showed that for the B_2-coil, it is not possible to create a measurable shift even with an optimistic current estimation of a few Amperes. Hence, this coil wasn't investigated further and will not be implemented in ELCOTRAP.

Also, different methods for joining the wires were investigated. To measure the field, an NVE AA005-02e magnet sensor was calibrated at a temperature of 4 K. A test setup for a

coldhead was developed to facilitate quick iteration cycles and allow testing of several joints. Additionally, the test setup was capable of inducing a high current through the joints. The NbTi wire joints tested in this thesis were fabricated using a Lampert PUK U5 spot welder, and joints were made for wires with a 0.3 mm diameter and wires with a 0.5 mm diameter. Two different approaches were examined: one where the wires were directly welded together, and another where both wires were welded inside a small NbTi cylinder.
All tested joints remained superconducting in a zero background magnetic field up to over 2.5 A for the 0.5 mm diameter wire and up to over 1.4 A for the 0.3 mm diameter wire. No significant difference was observed between the direct weld joints and those placed inside the cylinder. Similarly, the two wire diameters showed comparable performance, with no significant variation in results. The difference in currents was due to the different geometries used during the tests. Unfortunately, the setup was limited to the aforementioned currents, as the power supply could not provide higher currents, and none of the critical currents were reached.
Furthermore, the direct joint between the thin wire was tested in the 7 T background field of the ELCOTRAP experiment. A test coil containing the joint was wrapped around the trap chamber, where a $^{12}C^{6+}$ ion was stored. When a current was passed through the test coil, the resulting frequency shift of the particle was measured. The joint did not stay superconducting in this strong background field for reasons that were not fully investigated in the scope of this thesis due to time constraints. Further measurements are needed to solve the problem.
Lastly, a method for implementing the coil in ELCOTRAP was presented. A mount was developed that included a heater and a power supply, designed to minimize deviations from the ideal calculated geometry.

For future investigations, it would be interesting to use the developed setups to test other joining methods, such as cold-pressing or electromagnetic forming, as research on these techniques in strong background fields is still quite limited. Also, further research on possible reasons, why the joint in the strong background field did not examine superconductivity would be interesting. Additionally, a systematic investigation of the influence of different welding parameters would be valuable and could provide a deeper understanding of the welding process.
The next step is to manufacture and implement the B_0-coil in the experiment. Once installed, it can be tested to determine if everything functions as expected and if the desired frequency shifts are achieved. If successful, and the coupling in ELCOTRAP proves efficient, the new technique of sympathetic cooling of ions using electrons can be explored. This could pave the way for a cooling method for ions that cannot be laser-cooled, potentially leading to increased accuracy in measurements of particle mass or g-factors.

Bibliography

[1] X. Fan et al. "Measurement of the Electron Magnetic Moment". In: *Phys. Rev. Lett.* 130 (7 Feb. 2023), p. 071801. DOI: 10.1103/PhysRevLett.130.071801. URL: https://link.aps.org/doi/10.1103/PhysRevLett.130.071801 (cit. on p. 1).

[2] C Smorra et al. "A parts-per-billion measurement of the antiproton magnetic moment". In: *Nature* 550.7676 (Oct. 2017), pp. 371–374 (cit. on p. 1).

[3] M. Dine and A. Kusenko. "Origin of the matter-antimatter asymmetry". In: *Rev. Mod. Phys.* 76 (1 Dec. 2003), pp. 1–30. DOI: 10.1103/RevModPhys.76.1. URL: https://link.aps.org/doi/10.1103/RevModPhys.76.1 (cit. on p. 1).

[4] K. Blaum. "High-accuracy mass spectrometry with stored ions". In: *Physics Reports* 425.1 (2006), pp. 1–78. ISSN: 0370-1573. DOI: https://doi.org/10.1016/j.physrep.2005.10.011. URL: https://www.sciencedirect.com/science/article/pii/S0370157305004643 (cit. on pp. 1, 4, 6–8).

[5] J. Ketter. "Theoretical treatment of miscellaneous frequency-shifts in Penning traps with classical perturbation theory". PhD thesis. Ruperecht-Karls-Universität, Heidelberg, 2015 (cit. on pp. 1, 6).

[6] K. Blaum, Y. N. Novikov, and G. Werth. "Penning traps as a versatile tool for precise experiments in fundamental physics". In: *Contemporary Physics* 51.2 (2010), pp. 149–175. DOI: 10.1080/00107510903387652. eprint: https://doi.org/10.1080/00107510903387652. URL: https://doi.org/10.1080/00107510903387652 (cit. on p. 3).

[7] J. Dilling et al. "Penning-Trap Mass Measurements in Atomic and Nuclear Physics". In: *Annual Review of Nuclear and Particle Science* 68.Volume 68, 2018 (2018), pp. 45–74. ISSN: 1545-4134. DOI: https://doi.org/10.1146/annurev-nucl-102711-094939. URL: https://www.annualreviews.org/content/journals/10.1146/annurev-nucl-102711-094939 (cit. on p. 3).

[8] S. Rau et al. “Penning trap mass measurements of the deuteron and the HD+ molecular ion”. In: *Nature* 585.7823 (Sept. 2020), pp. 43–47 (cit. on p. 3).

[9] E. G. Myers. “High-Precision Atomic Mass Measurements for Fundamental Constants”. In: *Atoms* 7.1 (2019). ISSN: 2218-2004. DOI: 10.3390/atoms7010037. URL: https://www.mdpi.com/2218-2004/7/1/37 (cit. on p. 3).

[10] T. Sailer et al. “Measurement of the bound-electron g-factor difference in coupled ions”. In: *Nature* 606.7914 (June 2022), pp. 479–483 (cit. on p. 3).

[11] A. Mooser et al. “A New Experiment for the Measurement of the g -Factors of 3 He + and 3 He 2+”. In: *Journal of Physics: Conference Series* 1138 (Nov. 2018), p. 012004. DOI: 10.1088/1742-6596/1138/1/012004 (cit. on p. 3).

[12] S. Earnshaw. “On the Nature of the Molecular Forces which Regulate the Constitution of the Luminiferous Ether”. In: *Transactions of the Cambridge Philosophical Society* (1848) (cit. on p. 3).

[13] J. Repp et al. “PENTATRAP: a novel cryogenic multi-Penning-trap experiment for high-precision mass measurements on highly charged ions”. In: *Applied Physics B* 107.4 (June 2012), pp. 983–996 (cit. on p. 4).

[14] G. Gabrielse, L. Haarsma, and S.L. Rolston. “Open-endcap Penning traps for high precision experiments”. In: *International Journal of Mass Spectrometry and Ion Processes* 88.2 (1989), pp. 319–332. ISSN: 0168-1176. DOI: https://doi.org/10.1016/0168-1176(89)85027-X. URL: https://www.sciencedirect.com/science/article/pii/016811768985027X (cit. on p. 4).

[15] M. Kretzschmar. “Particle motion in a Penning trap”. In: *European Journal of Physics* 12.5 (Sept. 1991), p. 240. DOI: 10.1088/0143-0807/12/5/010. URL: https://dx.doi.org/10.1088/0143-0807/12/5/010 (cit. on p. 5).

[16] R.X. Schüssler. “First High-Precision Mass Measurements at PENTATRAP on highly charged Xe and Re ions”. PhD thesis. Ruprecht-Karls-Universität, Heidelberg, 2019 (cit. on pp. 5, 6, 46).

[17] L. S. Brown and G. Gabrielse. “Geonium theory: Physics of a single electron or ion in a Penning trap”. In: *Rev. Mod. Phys.* 58 (1 Jan. 1986), pp. 233–311. DOI: 10.1103/RevModPhys.58.233. URL: https://link.aps.org/doi/10.1103/RevModPhys.58.233 (cit. on pp. 5, 7, 20).

[18] Blaum-Group. *F47- Cyclotron frequency in a Penning trap*. 2022 (cit. on p. 6).

[19] K. Blaum and A. Mooser. *Stored Charged Particles*. 2023 (cit. on pp. 6, 7).

[20] M. Höcker. “Precision Mass Measurements at THe-Trap and the FSU trap”. PhD thesis. Ruprecht-Karls-Universität, Heidelberg, 2016 (cit. on p. 6).

[21] M. Kretzschmar. "Single particle motion in a Penning trap: description in the classical canonical formalism". In: *Physica Scripta* 46.6 (Dec. 1992), p. 544. DOI: 10.1088/0031-8949/46/6/011. URL: https://dx.doi.org/10.1088/0031-8949/46/6/011 (cit. on p. 6).

[22] M. Vogel. *Particle confinement in Penning Traps*. Springer, 2022 (cit. on pp. 7, 9, 10).

[23] S. Ulmer. "First Observation of Spin Flips with a Single Proton Stored in a Cryogenic Penning Trap". PhD thesis. Ruprecht-Karls-Universtität, Heidelberg, 2011 (cit. on pp. 8, 10–12).

[24] M. Kretzschmar. "A quantum mechanical model of Rabi oscillations between two interacting harmonic oscillator modes and the interconversion of modes in a Penning trap". In: *AIP Conference Proceedings* 457.1 (Jan. 1999). ISSN: 0094-243X. DOI: 10.1063/1.57446. URL: https://www.osti.gov/biblio/21207932 (cit. on pp. 8, 19).

[25] M. König et al. "Quadrupole excitation of stored ion motion at the true cyclotron frequency". In: *International Journal of Mass Spectrometry and Ion Processes* 142.1 (1995), pp. 95–116. ISSN: 0168-1176. DOI: https://doi.org/10.1016/0168-1176(95)04146-C. URL: https://www.sciencedirect.com/science/article/pii/016811769504146C (cit. on p. 9).

[26] S. Djekic et al. "Temperature measurement of a single ion in a Penning trap". In: *The European Physical Journal D - Atomic, Molecular, Optical and Plasma Physics* 31.3 (Dec. 2004), pp. 451–457 (cit. on p. 9).

[27] M. Jensen, T. Hasegawa, and J. Bollinger. "Temperature Measurements of Laser-Cooled Ions in a Penning Trap, ed. by M. Schauer, T. Mitchell, and R. Nebel". en. In: 692 (Jan. 2003). URL: https://tsapps.nist.gov/publication/get_pdf.cfm?pub_id=105333 (cit. on p. 9).

[28] A. Dörr. "PENTATRAP: A novel Penning-trap system for high-precision mass measurements". PhD thesis. Ruprecht-Karls-Universität, Heidelberg, 2015 (cit. on pp. 10, 12).

[29] J. Herkenhoff. "Development of a Digital Feedback System for Advanced Ion Manipulation Techniques within a Penning Trap". Bachelor's Thesis. Bremen City University of Applied Sciences, 2020 (cit. on p. 10).

[30] W. Shockley. "Currents to Conductors Induced by a Moving Point Charge". In: *Journal of Applied Physics* 9.10 (Oct. 1938), pp. 635–636 (cit. on p. 11).

[31] X. Feng et al. "Tank circuit model applied to particles in a Penning trap". In: *Journal of Applied Physics* 79.1 (Jan. 1996), pp. 8–13 (cit. on p. 12).

[32] D. van Delft and P. Kes. "The discovery of superconductivity". In: *Physics Today* 63.9 (Sept. 2010), pp. 38–43 (cit. on p. 13).

[33] P. Mangin and R. Kahn. *Superconductivity*. Springer, 2017 (cit. on p. 13).

[34] B. B. Goodman. "Type II superconductors". In: *Reports on Progress in Physics* 29.2 (July 1966), p. 445. DOI: 10.1088/0034-4885/29/2/302. URL: https://dx.doi.org/10.1088/0034-4885/29/2/302 (cit. on p. 13).

[35] A. M. Forrest. "Meissner and Ochsenfeld revisited". In: *European Journal of Physics* 4.2 (Apr. 1983), p. 117. DOI: 10.1088/0143-0807/4/2/011. URL: https://dx.doi.org/10.1088/0143-0807/4/2/011 (cit. on p. 13).

[36] W. Martienssen and H. Warlimont. *Springer Handbook of Condensed Matter and Materials*. Springer, 2005 (cit. on p. 13).

[37] T. Boutboul et al. "Critical Current Density in Superconducting $Nb - Ti$ Strands in the 100 mT to 11 T Applied Field Range". In: *IEEE Transactions on Applied Superconductivity* 16.2 (2006), pp. 1184–1187. DOI: 10.1109/TASC.2006.870777 (cit. on p. 13).

[38] W. Tan. "Different Techniques of Producing Superconducting Joints and Methods of Joints Characterization". In: *Journal of Physics: Conference Series* 1635.1 (Nov. 2020), p. 012008. DOI: 10.1088/1742-6596/1635/1/012008. URL: https://dx.doi.org/10.1088/1742-6596/1635/1/012008 (cit. on p. 14).

[39] D. Patel et al. "Niobium-titanium (Nb-Ti) superconducting joints for persistent-mode operation". In: *Scientific Reports* 9.1 (Oct. 2019), p. 14287 (cit. on p. 14).

[40] J. Cheng et al. "Fabrication of NbTi Superconducting Joints for 400-MHz NMR Application". In: *IEEE Transactions on Applied Superconductivity* 22.2 (2012), pp. 4300205–4300205. DOI: 10.1109/TASC.2012.2185795 (cit. on p. 14).

[41] Z. Shen et al. "Fabrication and Test of Nb3Sn-NbTi Superconducting Joint for a 14-T MRI Magnet". In: *IEEE Transactions on Applied Superconductivity* 34.5 (2024), pp. 1–4. DOI: 10.1109/TASC.2023.3337325 (cit. on p. 14).

[42] J. Liu et al. "Electrical properties of cold-pressing welded NbTi persistent joints". In: *Cryogenics* 58 (2013), pp. 62–67. ISSN: 0011-2275. DOI: https://doi.org/10.1016/j.cryogenics.2013.09.011. URL: https://www.sciencedirect.com/science/article/pii/S0011227513000945 (cit. on p. 14).

[43] J. Cheng et al. "Development of Electromagnetic Forming NbTi Superconducting Joint". In: *IEEE Transactions on Applied Superconductivity* 26.7 (2016), pp. 1–5. DOI: 10.1109/TASC.2016.2593943 (cit. on p. 14).

[44] W. Sun et al. “Preparation and Properties of NbTi–Nb3Sn–NbTi Superconducting Joints”. In: *Journal of Low Temperature Physics* 213 (Aug. 2023), pp. 1–13. DOI: 10.1007/s10909-023-02995-x (cit. on p. 14).

[45] J. Hafstrom et al. “Joining NbTi superconductors by ultrasonic welding”. In: *IEEE Transactions on Magnetics* 13.1 (1977), pp. 94–96. DOI: 10.1109/TMAG.1977.1059416 (cit. on p. 14).

[46] G. D. Brittles et al. “Microstructural Properties and Magnetic Testing of Spot-Welded Joints Between Nb–Ti Filaments”. In: *IEEE Transactions on Applied Superconductivity* 26.3 (2016), pp. 1–4. DOI: 10.1109/TASC.2016.2529290 (cit. on p. 14).

[47] J. A. Devlin et al. “Superconducting Solenoid System with Adjustable Shielding Factor for Precision Measurements of the Properties of the Antiproton”. In: *Phys. Rev. Appl.* 12 (4 Oct. 2019), p. 044012. DOI: 10.1103/PhysRevApplied.12.044012. URL: https://link.aps.org/doi/10.1103/PhysRevApplied.12.044012 (cit. on p. 14).

[48] J. D. Jackson. *Klassische Elektrodynamik*. Berlin, Boston: De Gruyter, 2014. ISBN: 9783110334470. DOI: doi:10.1515/9783110334470. URL: https://doi.org/10.1515/9783110334470 (cit. on p. 15).

[49] W. Braunbek. “Die Erzeugung weitgehend homogener Magnetfelder durch Kreisströme”. In: *Eur. Phys. J. A* 88.5-6 (May 1934), pp. 399–402 (cit. on pp. 15, 16).

[50] J. C. Maxwell. *A Treatise on Electricity and Magnetism*. Cambridge Library Collection - Physical Sciences. Cambridge University Press, 2010 (cit. on p. 16).

[51] J. F. Goodwin et al. “Resolved-Sideband Laser Cooling in a Penning Trap”. In: *Phys. Rev. Lett.* 116 (14 Apr. 2016), p. 143002. DOI: 10.1103/PhysRevLett.116.143002. URL: https://link.aps.org/doi/10.1103/PhysRevLett.116.143002 (cit. on p. 17).

[52] G. Savard et al. “A new cooling technique for heavy ions in a Penning trap”. In: *Physics Letters A* 158.5 (1991), pp. 247–252. ISSN: 0375-9601. DOI: https://doi.org/10.1016/0375-9601(91)91008-2. URL: https://www.sciencedirect.com/science/article/pii/0375960191910082 (cit. on p. 17).

[53] F. Herfurth et al. “A linear radiofrequency ion trap for accumulation, bunching, and emittance improvement of radioactive ion beams”. In: *Nuclear Instruments and Methods in Physics Research Section A: Accelerators, Spectrometers, Detectors and Associated Equipment* 469.2 (2001), pp. 254–275. ISSN: 0168-9002. DOI: https://doi.org/10.1016/S0168-9002(01)00168-1. URL: https://www.sciencedirect.com/science/article/pii/S0168900201001681 (cit. on p. 17).

[54] W. M. Itano et al. "Cooling methods in ion traps". In: *Physica Scripta* 1995.T59 (Jan. 1995), p. 106. DOI: 10.1088/0031-8949/1995/T59/013. URL: https://dx.doi.org/10.1088/0031-8949/1995/T59/013 (cit. on p. 17).

[55] M. Vogel et al. "Resistive and sympathetic cooling of highly-charged-ion clouds in a Penning trap". In: *Phys. Rev. A* 90 (4 Nov. 2014), p. 043412. DOI: 10.1103/PhysRevA.90.043412. URL: https://link.aps.org/doi/10.1103/PhysRevA.90.043412 (cit. on p. 17).

[56] M. Hobein et al. "Evaporative Cooling and Coherent Axial Oscillations of Highly Charged Ions in a Penning Trap". In: *Phys. Rev. Lett.* 106 (1 Jan. 2011), p. 013002. DOI: 10.1103/PhysRevLett.106.013002. URL: https://link.aps.org/doi/10.1103/PhysRevLett.106.013002 (cit. on p. 17).

[57] M. S. Longair. *High Energy Astrophysics*. 2nd ed. Cambridge University Press, 1994 (cit. on p. 18).

[58] N. Evetts et al. "Open microwave cavity for use in a Purcell enhancement cooling scheme". In: *Review of Scientific Instruments* 87.10 (Oct. 2016), p. 104702 (cit. on p. 18).

[59] G. Gabrielse and H. Dehmelt. "Observation of inhibited spontaneous emission". In: *Phys. Rev. Lett.* 55 (1 July 1985), pp. 67–70. DOI: 10.1103/PhysRevLett.55.67. URL: https://link.aps.org/doi/10.1103/PhysRevLett.55.67 (cit. on p. 19).

[60] A. P. Povilus. "Cyclotron-Cavity Mode Resonant Cooling in Single Component Electron Plasmas". PhD thesis. University of California, Berkeley, Jan. 2015 (cit. on p. 19).

[61] L. Beal et al. "GEKKO Optimization Suite". In: *Processes* 6.8 (2018), p. 106. DOI: 10.3390/pr6080106 (cit. on p. 24).

[62] W. E. Hart, J.-P. Watson, and D. L. Woodruff. "Pyomo: modeling and solving mathematical programs in Python". In: *Mathematical Programming Computation* 3.3 (2011), pp. 219–260 (cit. on p. 24).

[63] Gurobi Optimization, LLC. *Gurobi Optimizer Reference Manual*. 2024. URL: https://www.gurobi.com (cit. on p. 24).

[64] P. Virtanen et al. "SciPy 1.0: Fundamental Algorithms for Scientific Computing in Python". In: *Nature Methods* 17 (2020), pp. 261–272. DOI: 10.1038/s41592-019-0686-2 (cit. on p. 24).

[65] D. J. Wineland and H. G. Dehmelt. "Principles of the stored ion calorimeter". In: *Journal of Applied Physics* 46.2 (Feb. 1975), pp. 919–930. ISSN: 0021-8979. DOI: 10.1063/1.321602. eprint: https://pubs.aip.org/aip/jap/article-pdf/46/2/919/18369766/919_1_online.pdf. URL: https://doi.org/10.1063/1.321602 (cit. on p. 25).

[66] NVE Corporation. *NVE Online Store*. Accessed: 2024-09-08 (cit. on p. 31).

[67] S A Elrod, J R Miller, and L Dresner. "The Specific Heat of NbTi from 0 to 7 T Between 4.2 and 20 K". In: *Advances in Cryogenic Engineering Materials*. Ed. by R P Reed and A F Clark. Boston, MA: Springer US, 1982, pp. 601–610 (cit. on p. 33).

[68] Lake Shore cryotronics. *Cryogenic wire specifications*. Accessed: 2024-08-28 (cit. on p. 44).